NTNU

Norwegian University of
Science and Technology

# Machine learning assisted low-frequency model building for AVO inversion

Amaury Alejandro Toloza Lara

Petroleum Geosciences
Submission date: June 2018
Supervisor: Per Åge Avseth, IGP
Co-supervisor: Alexsey Stovas, IGP

Norwegian University of Science and Technology
Department of Geoscience and Petroleum

# Abstract

AVO inversion is a valuable tool to estimate absolute reservoir properties from prestack seismic data. The bandwidth limitation of the seismic requires that the missing low frequencies must be added to the inversion in order to estimate absolute values. The standard method is to build a low-frequency model by interpolating and extrapolating low-pass filtered well logs guided by interpreted horizons, which often leads to artifacts and has no geologic insight. Artifacts and uncertainties in the low-frequency model manifest themselves in the inverted estimates, leading to incorrect interpretations and bad business decisions. In this study, an innovative methodology is proposed based on machine learning to find the non-linear relationship between seismic attributes and logged elastic properties from available wells, then the relation is used to estimate the low-frequency content of a target property away from well control. Only relevant attributes with a justifiable physical relationship with target elastic properties were used, such as AVO attributes and relative impedance. The methodology was applied in a practical exploration case and validated for a true blind well location. Even though the statistical basis of the method becomes less robust in areas with very limited well availability, the results indicate that this methodology is able to estimate more accurately low-frequency content of elastic properties than the conventional method.

# Acknowledgment

I would like to thank my supervisor Per Avseth and Alexey Stovas for their expert advice, openness and support in this thesis. I would like to thank the people involved with PGS, Qeye Labs, and Rock Physics Technology for being diligent with the data delivery that was used in this work.

# Contents

# List of Figures

# List of Tables

# Chapter 1

# Introduction

Simultaneous AVO inversion has proven to be more effective at reservoir prospecting, characterization and providing significant risk reduction in business decisions than conventional poststack inversion and structural interpretation together (Kelly et al., 2001; Skidmore et al., 2001). The method exploits the amplitude variation with offset (AVO) to extract not only P-wave information but S-wave information as well from prestack seismic amplitudes (Ma, 2002). S-waves mainly interact with the rock matrix, whereas P-wave is far more sensitive to fluid changes, hence S-wave information enhances lithology and pore fluid discrimination. The increased discriminating capabilities have made simultaneous AVO inversion a routine tool for a variety of reservoir seismic applications (e.g., Li-ping and Han-ming, 2014; Chen et al., 2015; Yenwongfai et al., 2017a).

Even though simultaneous AVO inversion has the potential to be a useful direct hydrocarbon indicator, it suffers from uncertainties and pitfalls as discussed by Avseth et al. (2016). Assuming high quality seismic and well data, the inversion process uncertainties are the ones that affect inversion result the most. There are two fundamental limitations related to simultaneous AVO inversion (Mallick and Fu, 2007). First, the methodology assumes that the reflection amplitudes on prestack data can be described by the Zoeppritz equations or a linear approximation to these equations, normally based on the work of Aki and Richards (1980). The approximations assume small property contrasts and small angles of incidence. Any violation of these assumptions will lead to inadequate and misleading approximations. They hold true for angles of incidence up to 30°-40° for typical contrasts in elastic properties (Li et al., 2007). Second, the missing low frequencies required to estimate absolute elastic properties are added from derived low-frequency models that are assumed to adequately

describe the low-frequency content of the subsurface for the entire range of seismic data. Estimates from simultaneous AVO inversion give confident results using robust low-frequency models and limited angles of incidence even if seismic quality is rather poor (Veeken et al., 2004).

The first limitation can be overcome by AVO feasibility studies and limiting the maximum angle of incidence in angle gathers as suggested by Avseth et al. (2016). The second limitation is much more complex, given that uncertainties in the low-frequency model will propagate into the inversion results (Ball et al., 2015). The standard method to build low-frequency models is a simple interpolation/extrapolation of low-pass filtered elastic parameters from available well logs, constrained within a structural (faults) and stratigraphic (horizons) framework (Sams and Carter, 2017). The problem with this method is that it does not have any geological insight and the results are strongly dependent on the well data distribution. Under these circumstances, low-frequency models are unreasonable away from well control. This fact can negatively bias the absolute estimates and lead to incorrect interpretations, no matter how good the seismic quality is or how good seismic reflections can be described by AVO theory (Özdemir, 2009). Recently, the concept of joint impedance-facies inversion has emerged (e.g., Rimstad et al., 2012; Kemper and Gunning, 2014; Pendrel, 2015), where rock physics per facies information is implemented in a Bayesian framework to invert for elastic properties per facies without the need of a low-frequency model. However, simultaneous AVO inversion is still widely used in reservoir characterization and hydrocarbon exploration.

The main motivation of this study is to propose a methodology for low-frequency model building that overcomes the limitations of the traditional method. In this approach, multivariate linear regression is coupled with machine learning to establish a statistical relationship between available well log data and seismic attributes. The methodology is based on the work done by Hampson et al. (2001). The multivariate transform concept has been used as an alternative to seismic inversion (e.g., Keynejad et al., 2017; Yenwongfai et al., 2017b). The proposed methodology uses the multivariate transform concept differently. It is complementary to the simultaneous AVO inversion instead of an alternative. It is aimed to build more robust low-frequency models for more reliable absolute estimates from simultaneous AVO inversion results. It is worthwhile to build more robust low-frequency models because it will result in better business decisions.

The use of multivariate regression for low-frequency model building was first implemented by Hansen et al. (2008). In this study, least-squares multilinear regression is used to estimate the low-frequency model of acoustic impedance in an area with sparse well log data. TWT, time thickness, amplitude, interval velocity, and coherence attributes were used in the training data. Even though coherence and time thickness attributes carry some geological insight, it is difficult to relate them to acoustic impedance. There are two set of attributes that are missing in this study that better relate to acoustic impedance: relative acoustic impedance and AVO attributes (Cooke et al., 1999). The fit between estimated and measured low-pass filtered acoustic impedance at blind well locations is still excellent in the study.

Xia et al. (2012) and Zou et al. (2013) make use of relative impedance in a iterative approach coupled with seismic velocities. An initial model is built using seismic velocities and Gardner's equation. A second model is derived by multilinear regression using the initial model as attribute, along with conventional poststack seismic attributes. The second model is then used to invert for relative impedance. The final model is derived by multilinear regression using the now available inverted relative impedance and the second model. Relative impedance can be derived without the need of an initial model, avoiding the need to iterate (Lancaster and Whitcombe, 2000).

One of the issues with seismic velocities is that the upper limit of reliable information is hardly higher than 2 Hz (Cerney and Bartel, 2007). Ray and Chopra (2015) avoid the use of seismic velocities in another approach, and instead use a low-frequency model built by extrapolating a single well as an attribute, along with relative impedance and conventional poststack seismic attributes in a multilinear regression scheme.

The proposed method in this study represents a significant improvement to the existing methods. First of all, all existing methods use only multilinear regression schemes. Multilinear regression is only used for best attribute selection on the proposed approach and then it is cascaded to a probabilistic neural network. Neural networks capture non-linear relationships better, yielding better estimates in contexts where well data is sparse (Leiphart and Hart, 2001). Low-frequency models built by interpolation/extrapolation using a single well are used as attributes. Finally, prestack AVO attributes are included too as seismic attributes to the training data. These attributes have well defined relations to different reservoir properties.

# Chapter 2

# Theoretical background

## 2.1 Amplitude Variation with Offset

Amplitude versus offset is an important tool in quantitative seismic interpretation for hydrocarbon prediction and reservoir characterization. It is very popular in the oil industry since the seismic amplitudes for all offsets can be physically explained in terms of rock properties. In this section, the theoretical framework of AVO is reviewed in order to understand the assumptions, limitations, and pitfalls of this tool.

When a plane wave hit a rock interface at an oblique angle, partitioning of the incident energy occurs at the interface. Not only reflection and transmission of P-wave but also P- to S-mode conversion takes place. Below critical angle, an incident P-wave gives rise to a reflected P-wave, transmitted P-wave, reflected S-wave, and a transmitted S-wave (figure 2.1). The angular relationships among these components are explained by the Snell's law:

$$\frac{sin(\theta_r)}{V_{P_1}} = \frac{sin(\theta_t)}{V_{P_2}} = \frac{sin(\varphi_r)}{V_{S_1}} = \frac{sin(\varphi_t)}{V_{S_2}} \tag{2.1}$$

where $V_P$ and $V_S$ are the P- and S- wave velocities respectively for two media divided by an interface. The angles are measured from the normal. $\theta_r$ and $\theta_t$ are the angle of reflection and the angle of transmission respectively for the P-waves, $\varphi_r$ and $\varphi_t$ are the angle of reflection and the angle of transmission respectively for the S-waves. The partitioning of incident wave energy into the different components depends on the angle of incidence and on the properties contrasts of the two media.

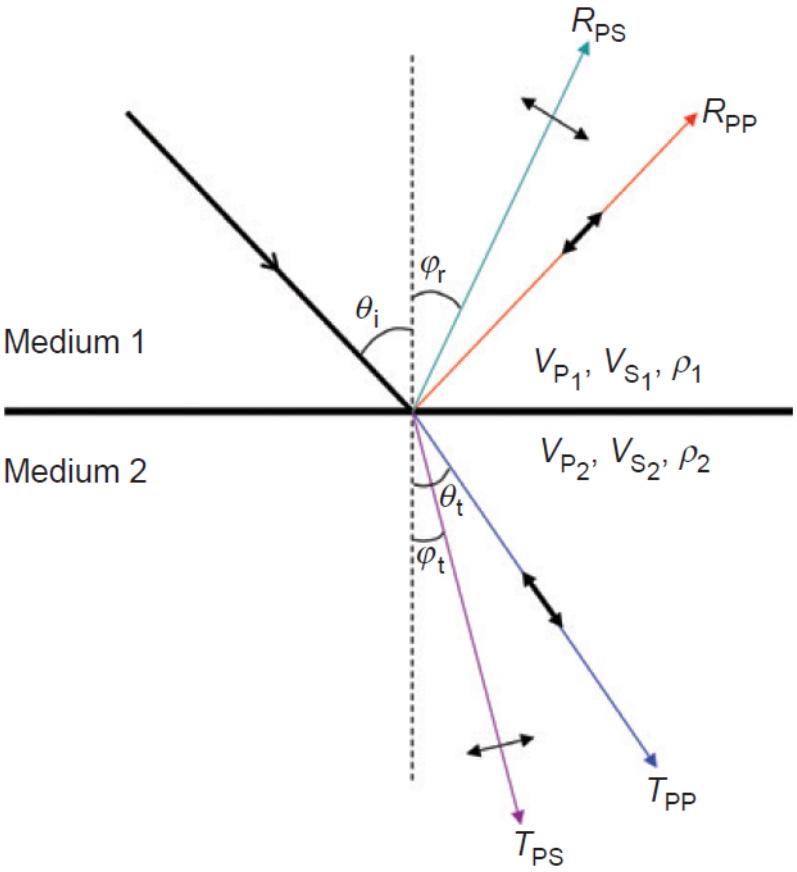


**Figure 2.1:** Energy partitioning for a plane wave that is incident on an interface. $V_P$, $V_P$, and $\rho$ are the P-wave velocity, S-wave velocity, and density respectively. The subscripts indicate the medium. The angle $\theta_i$ is the angle of incidence which is also equal to the angle of reflection for the P-reflected ray, $R_{PP}$. The angle $\theta_t$ is the angle of transmission for the P-transmitted ray, $T_{PP}$. Similarly, $\varphi_r$ and $\varphi_t$ are the angle of reflection and the angle of transmission for the S-reflected ray, $R_{PS}$, and the S-transmitted ray, $T_{PS}$, respectively (from Chopra and Castagna, 2014).

### 2.1.1 Zoeppritz equations

The Zoeppritz equations are the set of equations that describe the energy partitioning of a seismic wave at an interface. Most AVO analysis techniques used today are based on the Zoeppritz equations or an approximation of it. Zoeppritz original equations are mathematical statements of boundary conditions. However, the equations can be conveniently written as matrix equations. Following Aki and Richards (1980), the equations for incident P-wave

reflection and transmission coefficients $R_{PP}$, $R_{PS}$, $T_{PP}$ and $T_{PS}$ are expressed as follows:

$$\begin{pmatrix} cos(\theta_i) & \frac{V_{P_1}}{V_{S_1}} sin(\varphi_r) & \frac{V_{P_1}}{V_{P_2}} cos(\theta_t) & -\frac{V_{P_1}}{V_{S_1}} sin(\varphi_r) \\ -sin(\theta_i) & \frac{V_{P_1}}{V_{S_1}} cos(\varphi_r) & \frac{V_{P_1}}{V_{P_2}} sin(\theta_t) & \frac{V_{P_1}}{V_{S_1}} cos(\varphi_t) \\ -cos(2\varphi_r) & -sin(2\varphi_r) & \frac{\rho_2}{\rho_1} cos(2\varphi_t) & -\frac{\rho_2}{\rho_1} sin(2\varphi_t) \\ sin(2\theta_i) & -\frac{V_{P_1}^2}{V_{S_1}^2} cos(2\varphi_r) & \frac{\rho_2 V_{S_2}^2 V_{P_1}^2}{\rho_1 V_{S_1}^2 V_{P_2}^2} sin(2\theta_t) & \frac{\rho_2 V_{P_1}^2}{\rho_1 V_{S_1}^2} cos(2\varphi_t) \end{pmatrix} X \begin{pmatrix} R_{PP} \\ R_{PS} \\ T_{PP} \\ T_{PS} \end{pmatrix} = \begin{pmatrix} cos(\theta_i) \\ sin(\theta_i) \\ cos(2\varphi_r) \\ sin(2\theta_i) \end{pmatrix} \tag{2.2}$$

where $V_P$, $V_S$, and $\rho$ are the P-wave velocity, S-wave velocity, and density respectively. They carry a subscript 1 for medium 1 and subscript 2 for medium 2. The angle $\theta_i$ is the angle of incidence and also equal to the angle of reflection for $R_{PP}$, The angle $\theta_t$ is the angle of transmitted P-ray $T_{PP}$. Similarly, $\varphi_r$ and $\varphi_t$ are the angle of reflection and angle of transmission for the S-reflected ray $R_{PS}$, and the S-transmitted ray $T_{PS}$ respectively. The Zoeppritz equations (2.2) give the reflection and transmission coefficients for plane waves as a function of the angle of incidence and three independent parameters (density, P-wave, and S-wave velocities) of the two media on each side of the interface.

Chopra and Castagna (2014) mention certain characteristics of the Zoeppritz equation to be aware of. They describe plane-wave solutions where reflection and transmission coefficients are frequency independent. Actual seismic waves are spherical waves and exhibit frequency-dependent reflection coefficients. The Zoeppritz equations describe reflection coefficients in the direction of wave propagation, whereas for vertical geophones only the vertical component of the reflection response is of interest. It may not be the case for hydrophones that is omnidirectional. The Zoeppritz equations describe the reflection for a horizontal interface that separates two half-spaces; thus, they do not include wavelet-interference effects. They do not take into account transmission losses, attenuation, divergence, multiples, converted waves, seismic noise, etc. This has to be taken care of during seismic processing, otherwise, it can lead to highly misleading interpretations. Another assumption is that both materials are isotropic. There is strong evidence that shale can be anisotropic. There are anisotropic variations of the Zoeppritz equations and its approximations. Despite its limitations, Zoeppritz equations have proved to be useful to explain the seismic response in different combinations of rock properties. The most robust parameters that can be inferred from AVO are the contrast in impedance and Poisson's ratio.

### 2.1.2 Approximations to the Zoeppritz equations

The Zoeppritz equations are not simple and their solutions are laborious, they have a complicated dependence on elastic parameters of the two media, and on the angle of incidence. It is difficult to understand how a particular parameter affects the reflection-coefficient curve. To better understand the relationship between coefficients and the physical parameters at a given incidence angle, different approximate expressions have been developed over the years. A well-known approximation is given by Aki and Richards (1980):

$$R(\theta) \approx \frac{1}{2}\left(\frac{\Delta V_P}{V_P} + \frac{\Delta \rho}{\rho}\right) + \left(\frac{1}{2}\frac{\Delta V_P}{V_P} - 4\frac{V_S^2}{V_P^2}\frac{\Delta V_S}{V_S} - 2\frac{V_S^2}{V_P^2}\frac{\Delta \rho}{\rho}\right) \times sin^2(\theta) + \frac{1}{2}\frac{\Delta V_P}{V_P}(sin^2(\theta)tan^2(\theta)) \tag{2.3}$$

where

$$\begin{aligned} V_P &= \frac{V_{P2} + V_{P1}}{2}, \quad \Delta V_P = V_{P2} - V_{P1} \\ V_S &= \frac{V_{S2} + V_{S1}}{2}, \quad \Delta V_S = V_{S2} - V_{S1} \\ \rho &= \frac{\rho_2 + \rho_1}{2}, \quad \Delta \rho = \rho_2 - \rho_1 \end{aligned} \tag{2.4}$$

which is of the form

$$R(\theta) \approx A + Bsin^2(\theta) + Csin^2(\theta)tan^2(\theta) \tag{2.5}$$

where $A$ is called the AVO intercept, the zero-offset stack, or the "true" normal incidence reflectivity, $B$ is commonly referred to as the AVO slope or gradient and is a measure of the rate of change of the amplitude with time, and $C$ is called the curvature. For small angles, the third term is of fourth order and often neglected. As mentioned by Chopra and Castagna (2014), dropping the last term is desirable because it renders the equation linear in $sin^2(\theta)$. A linear equation is more robust than a parabolic one with three coefficients.

The assumptions for this approximation are that the contrasts of the properties on both sides of the interface are sufficiently small, and the angles of incidence are small too. The approximation is far worse at large incident angles and it breaks down as the angle approaches the critical angle. These assumptions, however, are reasonable and valid for many applications.

There are various approximations and most of them are based on algebraic rearranges of the Aki and Richards (1980) equation (2.3). It is outside of the scope of this work to review all of them, Li et al. (2007) summarize the most widely used approximations, the solution they

seek and their assumptions and limitations. The Fatti et al. (1994) approximation is relevant for this work since the AVO inversion algorithm used is based on this approximation. Fatti et al. (1994) rearrange the Aki and Richards (1980) equation (2.3) as follows:

$$R(\theta) \approx \frac{1}{2}(1 + tan^2(\theta))\frac{\Delta I_P}{I_P} - 4\left(\frac{V_S}{V_P}\right)^2 sin^2(\theta)\frac{\Delta I_S}{I_S} - \left[\frac{1}{2}tan^2(\theta) - 2\left(\frac{V_S}{V_P}\right)^2 sin^2(\theta)\right]\frac{\Delta\rho}{\rho} \quad (2.6)$$

Note that this equation solves for P- and S- impedance reflectivities. The third term is much smaller than the other two terms because $sin\theta \approx tan\theta$ for small angles and hence the third therm is very small even for large contrasts in density. This approximation is very intuitive when it comes down to understand why is difficult to determine density from AVO from low angles of incidence (Lines, 1998). Large angles of incidence are required for the third term to actually add some value. There a number of associated issues with wide angles mentioned by Roy et al. (2008) that also explains why is difficult to invert for density. The approximation makes no other assumption apart from the small contrasts in the elastic properties of the two medium, and the equation is good out to large precritical angles.

### 2.1.3 Classification of AVO responses

Castagna et al. (1998) proposed a classification (Table 2.1) on the basis of where the top of a gas sand falls in the intercept-versus-gradient crossplot (Figure 2.2). The reflection coefficient versus angle response is modelled for all classes in figure 2.3.

**Table 2.1:** AVO classes classification in terms of their position on the intercept versus gradient crossplot, and their sign associated with those attributes.

| Class | Relative impedance | Quadrant | $R(0)$ | $G$ |
|---|---|---|---|---|
| 1 | High-impedance sand | 4th | + | - |
| 2p | Near-zero impedance contrast | 4th | + | - |
| 2n | Near-zero impedance contrast | 3rd | - | - |
| 3 | Low-impedance sand | 3rd | - | - |
| 4 | Low-impedance sand | 2nd | - | + |

Class 1 anomalies occur when the acoustic impedance of the upper layer is less than that of the lower layer. Reflectivity is strong positive at zero offset and decreases in magnitude with offset and can change polarity at large offset. Because of this polarity change, the reflection response can cancel out in CMP stacking. They normally correspond to hard formations related to deep, well-consolidated sands.

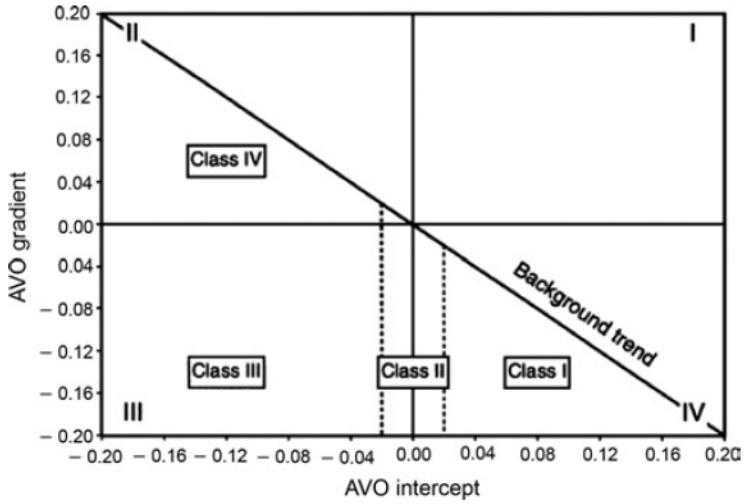


**Figure 2.2:** Crossplot of AVO intercept versus AVO gradient showing all four possible quadrants. Brine-saturated sandstones and shales tend to fall along a well-defined background trend. The top of the gas sand tend to fall below the background trend, whereas the bottom of the gas sand tend to fall above the background trend (from Castagna et al., 1998).

Class 2 anomalies response shows a very small difference in acoustic impedance between the upper and lower layer. The normal incident P-wave reflection coefficient is either slightly positive or slightly negative (2p or 2n respectively) with a strong negative gradient. They can appear as dim spots, bright spots, or polarity reversals on stacked seismic data.

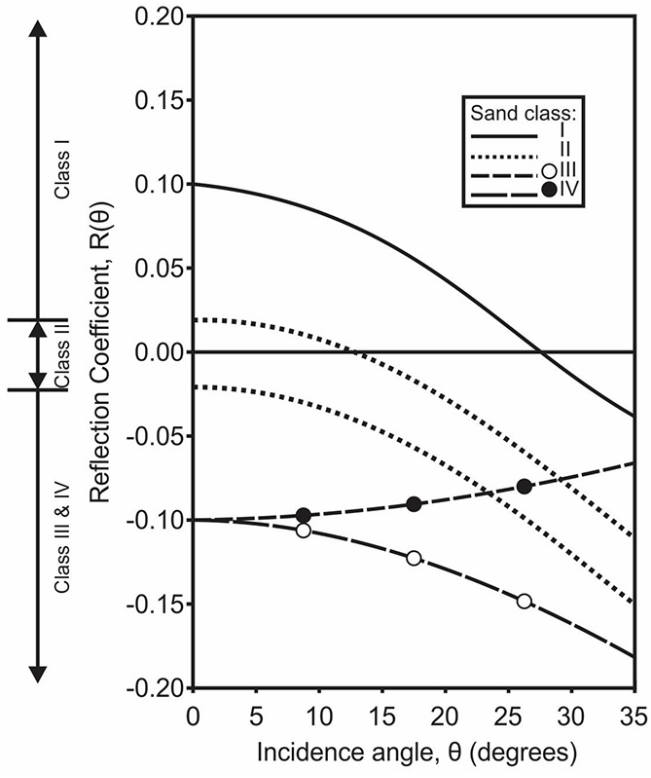


**Figure 2.3:** Reflection coefficients versus angle for all classes (from Castagna et al., 1998).

Class 3 response occurs where the acoustic impedance of the upper layer is higher than that of the lower layer. The normal incident P-wave reflection coefficient is strong negative with a negative gradient. Classical bright spots show this class in stacked sections. Relatively shallow unconsolidated sediments exhibit class 3 anomalies.

Class 4 are relatively rare. They occur for unconsolidated or soft sands below a hard cap rock such as a hard shale, or a carbonate. Large negative amplitude at zero offset and then decreases slightly with offset.

### 2.1.4 AVO attributes

Seismic attributes are measurements derived from seismic data, and they are useful because they correlate with physical properties of interest (Chopra and Marfurt, 2007). AVO attributes or pre-stack attributes are calculated based on the approximations of the Zoeppritz equations described in section 2.1.2. The two most important AVO attributes are Intercept or $I$ and Gradient or $G$ based on equation 2.5. Amplitudes are analyzed as a function of the squared sine of the estimated incidence angle and the algorithm fits a line in a least square sense where the slope of the line is the AVO gradient and its intersection of the amplitude axis is the AVO intercept (Rüger, 2002). The relation between these attributes and reservoir properties is given by:

$$I = \frac{1}{2}\left(\frac{\Delta V_P}{V_P} + \frac{\Delta \rho}{\rho}\right) \tag{2.7}$$

$$G = \left(\frac{1}{2}\frac{\Delta V_P}{V_P} - 4\frac{V_S^2}{V_P^2}\frac{\Delta V_S}{V_S} - 2\frac{V_S^2}{V_P^2}\frac{\Delta \rho}{\rho}\right) \tag{2.8}$$

it can be noticed that any change in the intercept is a function of the change of P-wave velocity or density or both, subsequently, any change in intercept would be directly correlated with a change in acoustic impedance $Z = V_P\rho$. The same is true for $G$ but in this case, the relation is more complex. Combinations of these two attributes are used to create other attributes. The AVO product is another common AVO attribute given by the product $I \times G$. Recalling table 2.1 is it evident that this attribute will highlight AVO class III anomalies very well, those are associated with soft sands with hydrocarbons or a classic bright spot. These sands will have a strong negative intercept and a strong negative gradient. The product will be a strong positive. Other classes will be weak or have negative products. On the down site, the AVO product is not able to recognize any other class but class III.

Wiggins et al. (1983) derived the relation $R_S \approx (I - G)/2$ where $R_S = \frac{1}{2}\left(\frac{\Delta V_S}{V_S} + \frac{\Delta \rho}{\rho}\right)$. The approximation is exact for $\frac{V_P}{V_S} = 2$. This attribute is called Scaled S-wave reflectivity and its general form $\alpha I - \beta G$. Following Wiggins et al. (1983), Castagna and Smith (1994) derived a similar relation, $R_P - R_S \approx (I + G)/2$ where $R_S = \frac{1}{2}\left(\frac{\Delta V_S}{V_S} + \frac{\Delta \rho}{\rho}\right)$ and $R_P = \frac{1}{2}\left(\frac{\Delta V_P}{V_P} + \frac{\Delta \rho}{\rho}\right)$. The approximation is exact for $\frac{V_P}{V_S} = 2$ too. A calibration is suggested in the form $\alpha I + \beta G$ to calibrate amplitudes and remove petrophysical biases. This attribute is later referred to as Scaled Poisson's reflectivity (Ross, 2002). Castagna and Smith (1994) demonstrated that it is an excellent hydrocarbon indicator in siliciclastic environments. The relation is based on that pore-fluid

changes will affect $R_P$ much more than $R_S$ whilst the porosity and lithology changes will affect them similarly. Hence, the reflection difference trends to cancel out lithology and porosity variations, while fluid changes are enhanced. This attribute will always be negative for gas sands and more negative than brine sands.

Scaled Poisson's reflectivity is equivalent to another attribute defined by Smith and Gidlow (1987) as the fluid factor. It is defined as the difference between observed $\frac{\Delta V_P}{V_P}$ and $\frac{\Delta V_P}{V_P}$ predicted from the Mudrock Line (Castagna et al., 1985). Fatti et al. (1994) redefined the fluid factor in terms of P-wave reflectivity and S-wave reflectivity. Any fluid change will other than brine will create a difference. Brine saturated lithology will cancel out.

Far vs near stack attributes can be useful when offset stacks are available. The far minus near stack is a rough estimate of an AVO gradient, and it is found to be a good attribute to detect class II AVO anomalies (Ross and Kinman, 1995). Other attributes include far minus near times far and far minus near times near. The first is a good attribute to enhance class II AVO anomalies. The second is a good attribute to enhance hydrocarbon-related class III AVO anomalies and reduce brine-saturated class II AVO response. More recent studies have developed AVO polarization attributes (Mahob and Castagna, 2003) that take into account wavelet characteristics. They mention these attributes are potentially useful hydrocarbon indicator and even enhances gas sands better than conventional AVO attributes. However, they will not work properly for poor signal-to-noise ratio in the seismic data and data with very low frequency data. There are many other AVO attributes but the ones previously mentioned are the most commonly used in AVO analysis.

### 2.1.5 AVO limitations

Some of the AVO limitations have already been mentioned. Nanda (2016) makes a summary of them. Firstly, the Zoeppritz's equations and their simplifications are the core of AVO analysis and inversion. They are valid under certain assumptions: Single horizontal interfaces assumption will not be valid for thin-bedded geology. Assumptions of plane waves instead of spherical waves, isotropy and frequency-independent reflection response are some factor that may affect adversely AVO analysis. Approximations to the Zoeppritz equation make other assumptions such as small contrasts in the media properties and limited angle of incidence. Any contexts where these assumptions are broken might lead to erroneous interpretations. Other limitations include composite events from overlapping reflections in complex

geology, presence of multiples and noise, scattering and absorption, tunning and interference effects, attenuation, transmission loss, incorrect NMO, etc.

There are many things that can affect the AVO estimates that makes it a complex and not very robust technology. Proper processing of seismic data can account for improved signal-to-noise ratio, acquisition footprints removal, correct amplitude balancing, enhanced signal bandwidth, multiple removal, attenuation and absorption compensation and so on, yet in complex situations, the data might not be of desirable quality. Final judgment is based on AVO modeling, geological understanding, rock physics, petrophysics, etc. Chopra and Castagna (2014) raise some practical questions for AVO analysis about its limitations and for the interpreter's awareness. Even if data quality is assured, the seismic response to fluid changes decreases with depth. It is known that AVO is useful within a range of depths called as the "AVO window" (Avseth et al., 2005).

## 2.2 Seismic Inversion and AVO

The concept of seismic inversion is better explained using the convolutional model. Seismic reflections on a zero-offset stack are represented from the convolution of reflection-coefficient series with a wavelet that characterizes the seismic source plus random noise (Cooke and Cant, 2010). Reflection coefficients are related to impedance contrasts between interfaces. Impedances are rock properties, not interface properties and these are calculated from density and velocity of the media. At the same time, density and velocity are related to many other rock properties such as porosity, fluid type, lithology, etc. Figure 2.4 represents the sketch of the convolutional seismic model or also known as seismic forward modelling, going from left to right. If the source wavelet is known, it can be deconvolved from the seismic, resulting in the reflection coefficient series. From right to left, it is the *inverse* of the seismic forward modeling. It extracts geological information from the seismic response (Chopra and Castagna, 2014), and that is the main reason of its popularity for reservoir characterization.

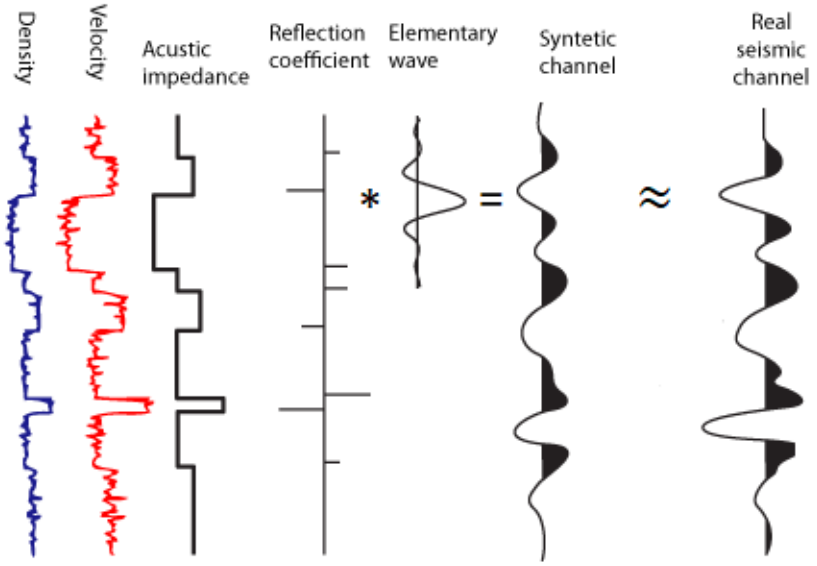


**Figure 2.4:** 1D Seismic convolutional model or seismic forward modelling concept .

Inversion methods can be classified into 4 categories: Deterministic vs Stochastic, Absolute vs Relative. They can have post- and pre-stack applications. There several different approaches in both categories. There is no clear consensus that any particular inversion algorithm is better than others and it can be argued that careful evaluation of every step taken is more important than the choice of the algorithm (Simm and Bacon, 2014). Each category is a wide topic. Outlining all inversion schemes is outside the scope of this study. Veeken et al. (2004) reviewed seismic inversion methods and some of their constraints in detail. There will be a particular focus on AVO inversion. It is important to mention that any inversion process has not a unique solution. That means that different geological configurations can have the same seismic response.

### 2.2.1 General principles of seismic inversion methods

Most available methods are based on the forward convolution of a reflectivity model with an estimated wavelet, a difference is computed between the modelled seismic and the observed seismic, then update the reflectivity model in order to minimize the difference between the modelled and observed seismic traces. Whether Generalized Linear Inversion, sparse spike or simulated annealing, all algorithms work on the principle of minimization (Schuster, 2017). Methods based on minimization are commonly known as 'deterministic'. Figure 2.5 shows a generic deterministic seismic inversion workflow.

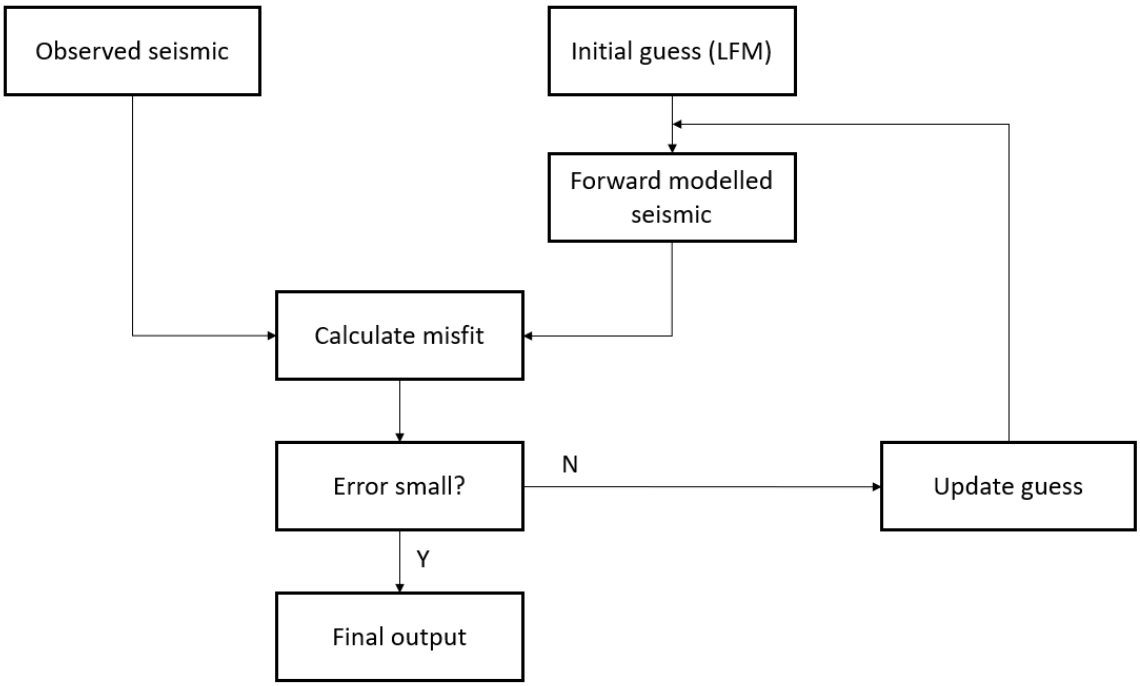


**Figure 2.5:** Generic deterministic inversion scheme.

On the other hand, stochastic seismic inversion generates a suite of alternative heterogeneous impedances representations that match the seismic within a certain threshold. Taken together, the suite of possible realization capture the uncertainty or non-uniqueness associated with the inversion process. Stochastic inversion is complementary to deterministic inversion. The deterministic seismic inversion is the average of all possible non-unique stochastic realizations (Francis, 2006).

### 2.2.2 Limitations of deterministic seismic inversion

Deterministic seismic inversion has some limitations. These arise because of the limited bandwidth of the seismic data. It is not widely appreciated that seismic inversion is non-unique because the seismic trace is band-limited. For a given inversion algorithm, the seismic inversion is unique within the seismic bandwidth. Band-limited or relative impedance inversion is possible without the need of a frequency model (Ball et al., 2014). Even though band-limited inversions have unique solutions, they are relative estimates and not absolute estimates of reservoir properties. The missing low frequencies contain critical information about the absolute values and without them only relative values can be obtained from seismic. The missing low frequency information must be added to the inversion in order

to obtain absolute values (Francis, 2006). This information is usually known as the Low-Frequency Model (LFM), and it constitutes the main limitation of any deterministic seismic inversion method. Figure 2.6 from Francis (2006) demonstrates this fact. A real data example for a relative inversion is compared to a high-pass filtered deterministic inversion. The differences are indistinguishable. This suggests that the low-frequency model offers very little value inside the content frequency of the seismic.

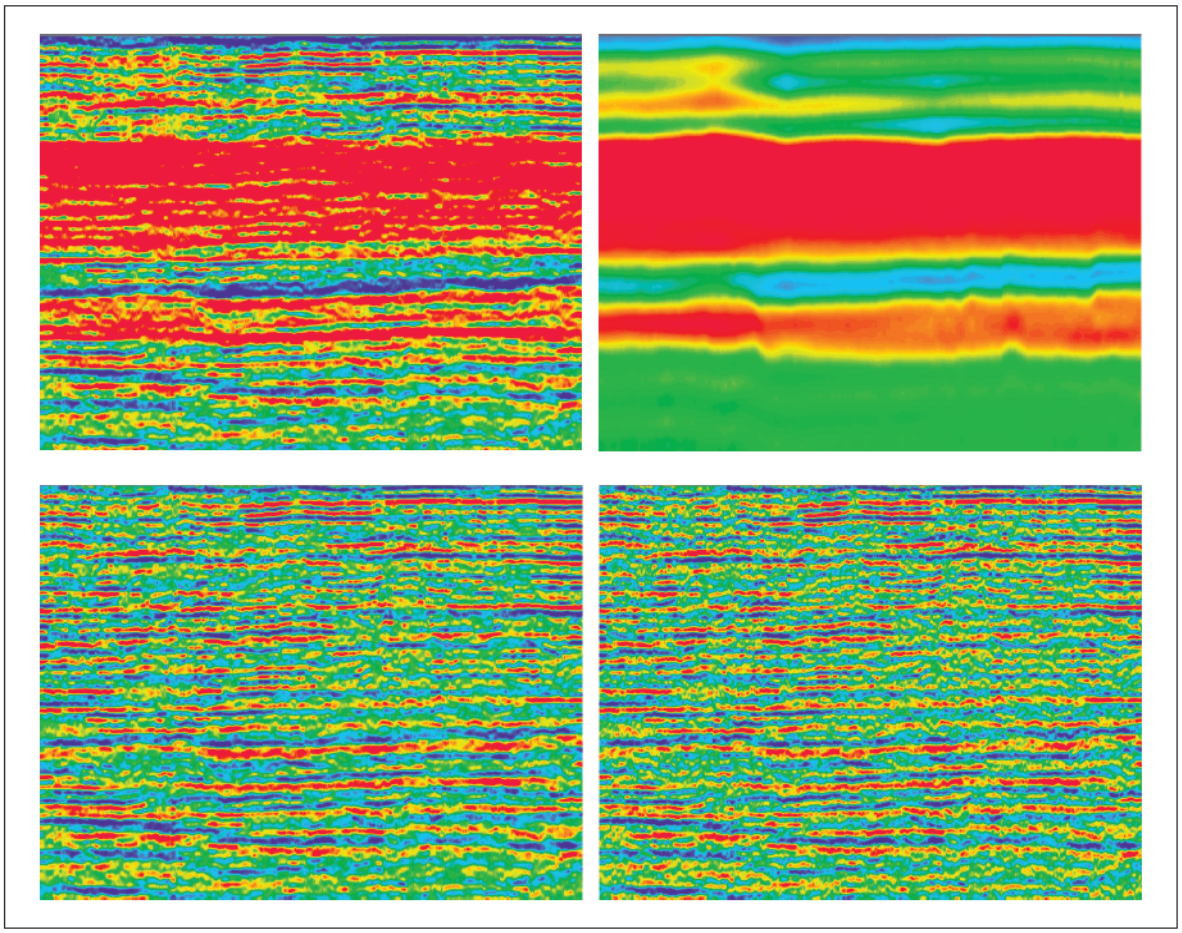

**Figure 2.6:** Deterministic inversion;top left: final seismic inversion;top right: low-pass filtered;lower left: high pass filtered;lower right: relative impedance.

The LFM controls the initial seismic guess, also constrains the non-uniqueness of the inversion method, stabilizing the process. Unreasonable low-frequency models can negatively bias absolute estimates and lead to incorrect interpretations (Sams and Carter, 2017). The more reliable estimate of the low frequency model, the more reliable estimates of absolute property values. This is the main focus of this work as stated in the introduction.

As it was mentioned in the introduction, a new approach has been developed to avoid the limitations of using a low-frequency model. Even though this new methodology is beyond

the scope of this study, it is important to mention it here. Francis (2010) already suggested that the limitations of using a low-frequency model can be avoided by adopting a stochastic inversion approach. Rimstad et al. (2012) and Kemper and Gunning (2014) recast the seismic inversion problem as a Bayesian problem. In order to account for the inadequate regularization and to capture the physics of the inverse problem properly, it is first inverted to facies and impedances per facies, then given those impedance it is inverted again for facies and so forth, until convergence. Only depth trends per facies are required as prior information, that means that the process of building a low frequency model is avoided.

The second biggest limitation is the wavelet estimation. It is straightforward to understand that for the same reflectivity series, its convolution with two different wavelets will result in two different seismic responses. The same is true in the inverse direction. Deconvolving the same seismic data with two different wavelets will result in two different reflectivities and hence in different property estimates. Figure 2.7 from Simm and Bacon (2014) shows how sensitive inversion can be to the wavelet used. The wavelets are quite similar to each other and yet there are observable differences in the inversion. All other parameters for the seismic inversion are the same.

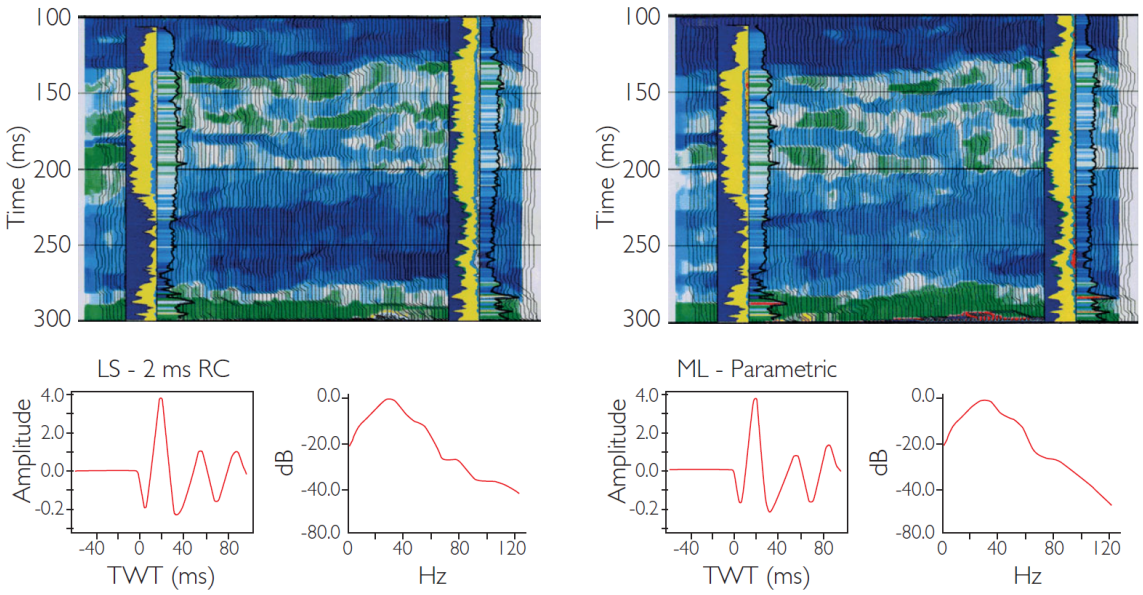


**Figure 2.7:** Sensitivity of inversion results to wavelets extracted from different methods.

### 2.2.3 Prestack seismic inversion

The convolutional model is the basis for poststack seismic inversion (figure 2.4). There is no mode conversion at normal incidence, then only P-wave impedance can be inverted from poststack seismic data. There is additional information in the prestack seismic data that is lost after stacking.

Methods that exploit amplitude variations versus offset from prestack seismic data are known as AVO inversion methods. AVO inversion methods can be divided into two categories: reflectivity methods and impedance methods (Russell, 2012). The first group of methods inverts for parameters associated with different approximations of the Zoeppritz equations, already described in section 2.1.2, such as Intercept, Gradient, Fluid Factor, among others also previously described (section 2.1.4). Methods that go beyond the estimation of AVO attributes and invert for elastic parameters, including $V_P$, $V_S$, and density are known as impedance methods. There are numerous impedance methods (e.g., Quakenbush et al., 2006; Goodway et al., 1997) but only the two most popular will be described in detail here.

#### Elastic impedance

Connolly (1999) introduced the concept of Elastic Impedance. First, the elastic impedance function is defined in terms of angle-dependent P-reflectivity assuming that it has to be analogous to the acoustic impedance, then

$$R(\theta) = \frac{F(t_i) - F(t_{i-1})}{F(t_i) + F(t_{i-1}} \tag{2.9}$$

where $F$ represents the elastic-impedance functions and $t$ is time. This can also be written as

$$R(\theta) = \frac{1}{2}\frac{\Delta EI}{EI} \approx \frac{1}{2}\Delta \ln(EI) \tag{2.10}$$

Where $EI$ is the elastic impedance or angle dependet impedance. This would be valid for small to moderate changes in impedance. Recalling equation 2.5 proposed by Aki and Richards (1980) given as

$$R(\theta) \approx A + Bsin^2(\theta) + Csin^2(\theta)tan^2(\theta)$$

combining the last two equations, and after integration and exponentiation the following

expression is obtained

$$EI = V_P^{(1+tan^2(\theta))} V_S^{(-8Ksin^2(\theta))} \rho^{(1-4Ksin^2(\theta))} \tag{2.11}$$

where $K = \frac{V_S^2}{V_P^2}$. It is easily demonstrable that $EI(0) = AI$. Inverting for elastic impedance gives information about shear wave velocity, that cannot be obtained from acoustic impedance.

In practice, a CMP gather at a well position is selected and different angle stacks are selected. Given that the log has $V_P$, $V_S$, and $\rho$ curves, elastic impedance is calculated for different angles of incidence. Angle-dependent reflectivity at well location is known, it is compared with the angle stacks and wavelet is derived. The derived wavelet is then deconvolved from the seismic volumes in the process of inverting angle stacks into elastic-impedance volumes. Whitcombe et al. (2002) further developed to the Extended Elastic Impedance that is shown to correlate better to various elastic parameters such as bulk modulus and lambda.

**Simultaneous inversion**

Simultaneous inversion refers to AVO extraction and estimation of elastic properties together. Ma (2002) combines these two processes into a single step and formulates the solution as a global optimization problem. Fatti et al. (1994) two terms approximation to the Zoeppritz equations is given by the expression

$$R(\theta) \approx \frac{1}{2}(1 + tan^2(\theta))\frac{\Delta I_P}{I_P} - 4\left(\frac{V_S}{V_P}\right)^2 sin^2(\theta)\frac{\Delta I_S}{I_S} \tag{2.12}$$

and is used to extract the P- and S- impedance reflectivities by fitting to the P-wave reflection amplitudes from real CMP gathers. Ma (2002) simplifies further by replacing $\frac{V_S}{V_P}$ by $\frac{I_S}{I_P}$ so reflection coefficients are only a function of $I_p$, $I_S$, and $\theta$, resulting in the following formula

$$R(\theta) \approx \frac{1}{2}(1 + tan^2(\theta))\frac{\Delta I_P}{I_P} - 4\left(\frac{I_S}{I_P}\right)^2 sin^2(\theta)\frac{\Delta I_S}{I_S} \tag{2.13}$$

where

$$\frac{\Delta I_P}{2I_P} = \frac{I_P^i - I_P^{i-1}}{I_P^i + I_P^{i-1}} \tag{2.14}$$

$$\frac{\Delta I_S}{2I_S} = \frac{I_S^i - I_S^{i-1}}{I_S^i + I_S^{i-1}} \tag{2.15}$$

$$\frac{I_S}{I_P} = \frac{I_S^i + I_S^{i-1}}{I_P^i + I_P^{i-1}} \tag{2.16}$$

For a given starting model, equation 2.13 can be solved to calculate the reflection coefficients $R(\theta)$. A synthetic seismic gather is computed by convolving the calculated reflection coefficients with predetermined wavelets. The synthetic data are compared with real observed data to form a misfit function. Each parameter is perturbed to form a new starting model which is used to generate a new synthetics data that is again compared to the observed data. This optimization loop is solved using simulated annealing to find a global minimum. The starting low-frequency model is used as a starting model and it reduces the non-uniqueness of the problem and stabilizes the algorithm.

The wavelets used for forward modelling of the synthetic data are calculated from multi-offset stacks. In this way, offset-dependent phase, bandwidth, tuning, and NMO stretch are captured in the wavelets (Pendrel et al., 2000).

## 2.3 Machine learning and reservoir properties prediction

There is yet another approach to estimate absolute reservoir properties from seismic. Those are based on the statistical relation between reservoir properties and the available data rather than the theoretical relation derived from the AVO theory described before. Diverse methods and algorithms fall into this category. The two most common ones used as predictor of reservoir properties are explained in detail here.

### 2.3.1 Multivariate Linear Regression

Multivariate linear regression is the extension of the conventional linear analysis to multiple variables (Neter et al., 1996). Under the context of this work, a target log can be expressed by the linear equation

$$L(t) = w_0 + w_1 A_1(t) + w_2 A_2(t) + w_3 A_3(t) + ... + w_n A_n(t) \tag{2.17}$$

where $t$ is time and $A_n$ are seismic attributes. The weights in the equation are derived by minimizing the mean-squared prediction error:

$$E^2 = \frac{1}{N}\sum_{i=1}^{N}(L_i - w_0 - w_1 A_{1i} - w_2 A_{2i} - w_3 A_{3i} - ... - w_n A_{ni})^2 \tag{2.18}$$

The frequency content of the target log is usually much higher than that of the seismic attribute as shown in figure 2.8. Correlating the log with the attributes on a sample-by-sample basis may not be optimal. The alternative is to assume that each sample on the target log is related to a group of neighboring samples on the seismic attribute as illustrated in figure 2.9 for convolution operator of 5 points. Hampson et al. (2001) demonstrates that the number of

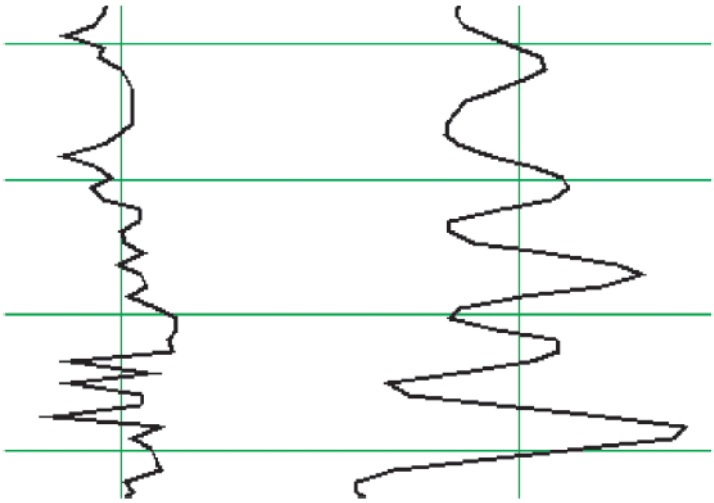

**Figure 2.8:** Comparison between the target log (left) and a seismic attribute (right) that lay stress on the frequency content difference (from Hampson et al., 2001).

coefficients from equation 2.17 increases to (number of attributes times convolutional operator length + 1) when a convolutional operator is used. They also show that the operator is equivalent to introducing time-shifted versions of the original attributes as new attributes.

### 2.3.2 Neural Networks

The disadvantage of multilinear analysis is that it is linear. Figure 2.10 illustrates the advantages of nonlinear transforms over linear transforms in the same data using just one attribute as an example. An option to derive nonlinear relationships is the use of neural networks.

Neural networks have been used for diverse geophysical problems. van der Baan and Jutten (2000) and Poulton (2002) provide a review of this tool for different geophysical applications. The idea of using neural networks and multiple seismic attributes to estimate

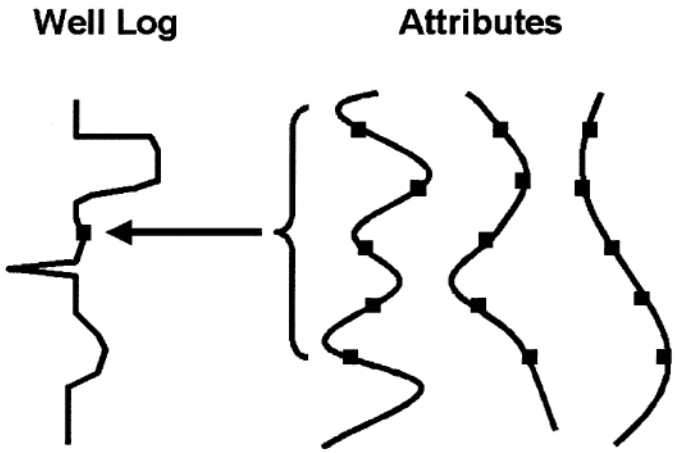


**Figure 2.9:** Example of five-point convolutional model to relate seismic attributes to a target log (from Hampson et al., 2001).

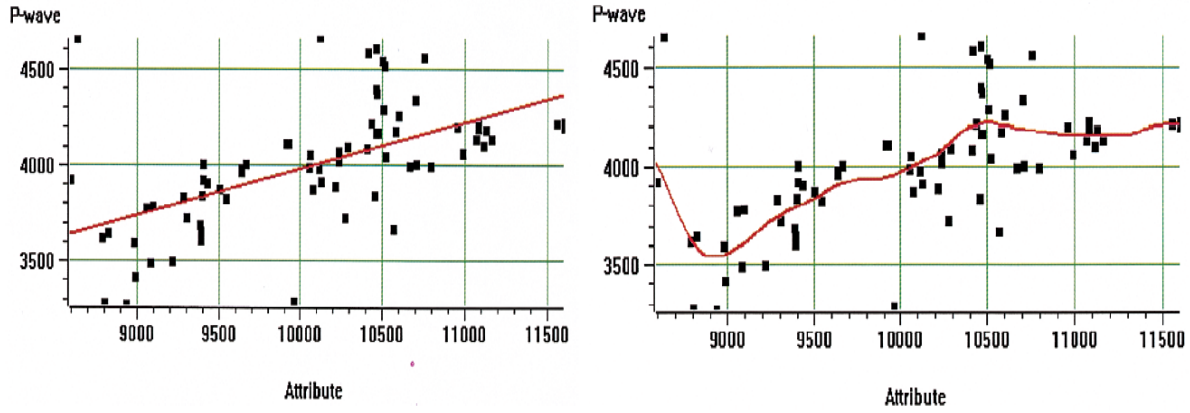


**Figure 2.10:** Linear analysis (left) vs Neural Network analysis (right) for the same data (from Hampson et al., 2001).

log properties away from well control was first introduced by Schultz et al. (1994). Further development and application of neural network to estimate reservoir properties have been done in recent years (e.g., Liu and Liu, 1998; Hampson et al., 2001; Banchs and Michelena, 2002; Herrera et al., 2006).

Different neural network schemes exist. Liu and Liu (1998) describe the use of a multi-layer feed-forward neural network (MLFN) for example. One issue with this type of implementation is explained by Hampson et al. (2001). MLFN can be overtrained easily, proposing the use of a probabilistic neural network or PNN instead.

The probabilistic neural network is actually a mathematical interpolation scheme that happens to use a neural network architecture for its implementation (Specht, 1990). The training data consist of seismic attribute values at well location plus the property log. An

example for three attributes can be written as follows

$$\{A_{1n}, \quad A_{2n}, \quad A_{3n}, \quad L_n\} \tag{2.19}$$

where there are $n$ training examples or well locations. Given the training data, the PNN assumes that each new output log value

$$x = \{A_{1j}, \quad A_{1j}, \quad A_{1j}\} \tag{2.20}$$

can be written as

$$L(x) = \frac{\sum_{i=1}^{n} L_i \exp\left(-D(x, x_i)\right)}{\sum_{i=1}^{n} \exp\left(-D(x, x_i)\right)} \tag{2.21}$$

where

$$D(x, x_i) = \sum_{j=1}^{3} \left( \frac{x_j - x_{ij}}{\sigma_j} \right)^2 \tag{2.22}$$

The quantity $D(x, x_i)$ is the distance between the input point and each of the training points $x_i$. This distance is measured in the multidimensional space spanned by the attributes and is scaled by $\sigma_j$, that can be different for each attribute. The training of the network consists of determining the optimal set of smoothing parameters $\sigma_j$. The criterion for determining these parameters is that the resulting network should have the lowest validation error.

### 2.3.3 Best attributes selection

Theoretically, an infinite number of seismic attributes could be used in multivariate regression. Practically, it would not only mean infinite processing time but it can cause overtraining, making the prediction to be worse outside the training data as described by Kalkomey (1997). Then, the problem is to select not only the proper attributes but the optimum number of attributes where neither under-training nor over-training occur.

A systematic procedure was developed by Hampson et al. (2001). The first single best attribute is found by exhaustive search, that means that all available attributes are used one by one and the prediction error is computed for all of them. The one with the lowest prediction error is the single best attribute. To find the best pair of attributes it is assumed that the single best one has to be one of them. A regression is performed and the prediction error is calculated where the first attribute is fixed and the second is a new attribute every time.

The best pair is the one with the lowest prediction error. The best triplet of attributes must have the best pair of attributes, then only the third attribute is checked for all other available attributes. The best triplet of attributes is again the one with lowest prediction error. This process can be repeated for to find the best $M$ attributes out of $N$ available attributes where $M < N$. This process is called step-wise regression.

The best $M$ attributes out of $N$ attributes could also be found by exhaustive search. In fact, the optimal solution might not be derived using step-wise regression. The problem with exhaustive search is that becomes computationally expensive very quickly. Even though step-wise regression might not lead to the optimal solution, it is a good solution. The computational time is reduced considerably and it already chooses attributes that are linearly independent as opposed to exhaustive search.

To determine the correct number of attributes to be used, Hampson et al. (2001) use the method of cross-validation. It consists of dividing the entire training data into two subsets: the training data and the validation data. The training data are used to calculate the multivariate transform, while the validation set is used to calculate the final prediction error. Over-training will result in a poorer fit to the validation data set. In this case, the division of the training data are all training samples from all wells, except a single hidden well which is the validation set. The analysis is repeated as many times as there are wells, each time leaving out a single different well. The total validation error is the RMS average of the individual errors:

$$E_V^2 = \frac{1}{N} \sum_{i=1}^{N} e_{Vi}^2 \tag{2.23}$$

where $E_V$ is the total validation error, $e_{Vi}$ is the validation error for well $i$, and $N$ is the number of wells in the analysis.

Figure 2.11 shows the validation error in red and the prediction error in black for the training data versus the number of attributes. The validation error is always higher than the training error because there is always one well less in the validation error that results in less predictive power. The training error always decreases because the higher number of attributes is analog to fitting a higher order polynomial. On the other hand, validation error does not decrease monotonically. It decreases and then gradually increases. The point where the validation error stops declining convincingly is the optimum number of attributes before over-training.

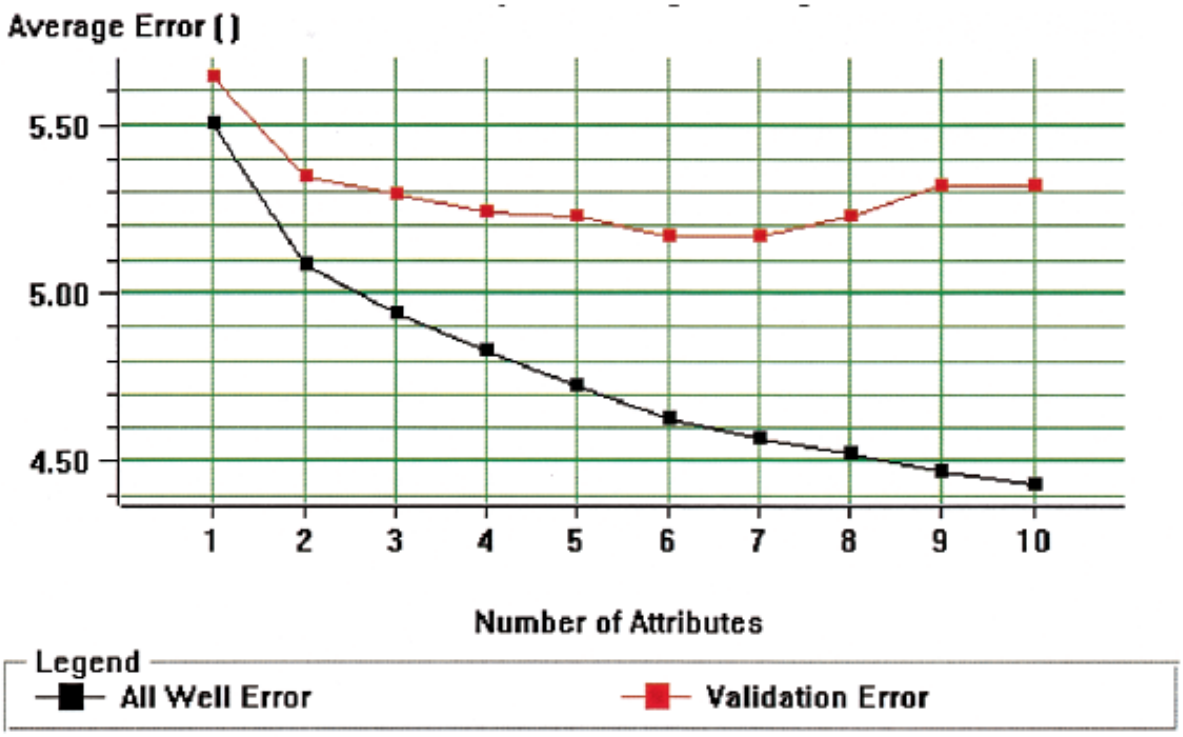


**Figure 2.11:** Validation error (red), and training error (black) versus number of attributes. Training error always decreases. The optimum number of attributes is 6 for this example (from Hampson et al., 2001).

### 2.3.4 Advantages and limitations

The main advantages of multivariate transforms are outlined by Hampson et al. (2001) and Herrera et al. (2006). It can predict any log in addition to acoustic and shear impedance, it may use any kind of seismic attributes, including seismic velocities and AVO attributes. It does not rely on any particular forward model and it does not require knowledge of the seismic wavelet, which are the two biggest limitations of prestack simultaneous inversion.

On the other hand, different authors have mentioned its limitations (e.g., Kalkomey, 1997; Banchs and Michelena, 2002; Ma, 2011; Ma and Gomez, 2015). The problem of under-training and over-training can be overcome by selecting the appropriate number of attributes. A systematic approach was described based on the work done by Hampson et al. (2001) but Banchs and Michelena (2002) agree that more research on this topic is needed. Kalkomey (1997) suggests that only seismic attributes that have a justifiable relationship with the target log should be considered as candidates for predictors. Its biggest limitation is that it is assumed that the training data spans the whole range of expected conditions in the subsurface. In other words, that the limited amount of samples is representative of the whole pop-

ulation of possible samples in the subsurface. This is directly linked to the number of wells and their distribution, the more well data and the better distributed it is, the more chances of capturing all the conditions in the subsurface. It is part of this work to evaluate how well this approach performs in a practical exploration case where there is limited number and distribution of well data.

# Chapter 3

# Methodology

In this chapter, all the steps that were applied in the proposed approach are explained in detail. Figure 3.1 gives an overview of the different steps followed in this study.

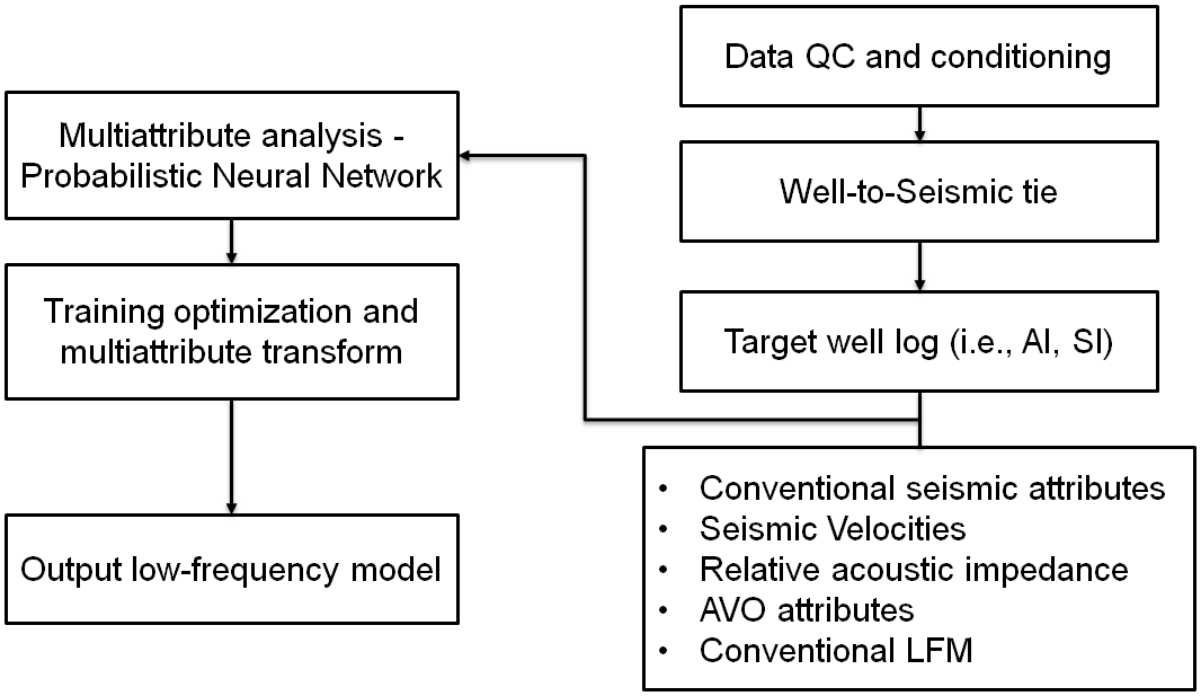


**Figure 3.1:** Methodology work-flow outline to build low-frequency models of elastic properties by means of multiattribute analysis

## 3.1 Gathers QC and stacking

## 3.2 Data

A comprehensive dataset was available for this work. A total of six wells were available within the extent of the available seismic. Corresponding well paths and check shots are available for the wells, with the exception of well 6507/11-11 that has no check shot. The well distribution is sparse, given it is an exploration setting. Figure 3.2 shows the location of the available wells within the seismic extent. The seismic is prestack migrated angle gathers conditioned for AVO in a 12.5 m X 12.5 m bin geometry. The angle range is from 3 to 48 degrees, and its time range is 1300 ms to 2796 ms. The final processing report is at disposal. The extension of the seismic can also be seen in figure 3.2. Reference Datum is ED50 UTM Zone 32.

Interpreted horizons for the Base Tertiary, Base Cretaceous Unconformity, Top Kai Formation, Top Garn Formation, and Intra Are Coal Marker were available as well. RMS velocity field from migration velocity analysis in a 50 m X 50 m grid was available too. It is later converted to interval velocities by means of Dix equation. Additional available information are sedimentology studies, prospect evaluation reports, well tops, drilling reports, Rock Physics and AVO feasibility studies.

Additional data are generated using the available data. These additional data comprises calculated acoustic and shear impedances logs, interval velocity field, relative acoustic impedance volume, AVO attributes, conventional seismic attributes and conventional low-frequency models. Their calculations are explained in detail in this chapter.

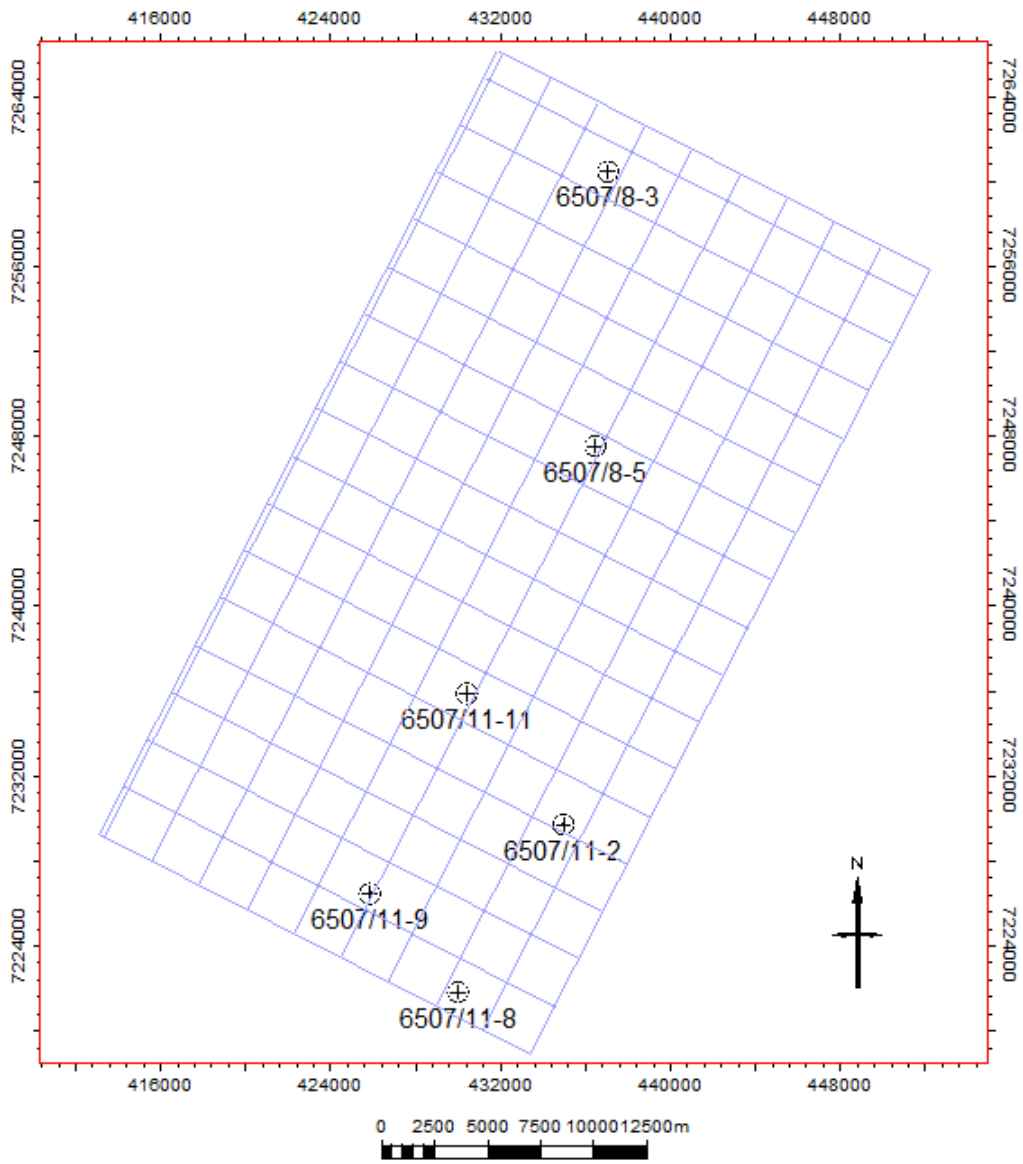


**Figure 3.2:** Wells location within the seismic extent.

## 3.3 Well log QC and conditioning

As it was mentioned before, a total of six wells are available. Table 3.1 comprises what logs are available for each available well. Even though only P-wave velocity, S-wave velocity, and density are required to calculate acoustic impedance, shear impedance, and Vp/Vs ratio, other logs such as gamma ray and caliper are extremely useful for QC and conditioning.

It is important to mention that only wells 6507/11-8, 6507/11-9, and 6507/11-11 have S-wave velocity, as it can be noted from table 3.1. This represents a serious limitation not only to conventional interpolation but also to the proposed methodology since it is very unlikely

**Table 3.1:** Available logs in the well database

| Well | Caliper | Density | Neutron | GR | P-wave | S-wave | Rsha | Rmed | Rdep |
|---|---|---|---|---|---|---|---|---|---|
| 6507/8-3 | X | X | X | X | X | | | X | X |
| 6507/8-5 | x | X | X | X | X | | | X | X |
| 6507/11-2 | X | X | X | X | X | | X | X | X |
| 6507/11-8 | X | X | X | X | X | X | X | X | X |
| 6507/11-9 | X | X | X | X | X | X | X | X | X |
| 6507/11-11 | X | X | X | X | X | X | X | X | X |

very few wells can capture all possible relations that can be encountered in the subsurface. P-wave velocity is present twice as much as S-wave velocity, hence Acoustic impedance will be better estimated than Shear impedance.

Well logs were imported for visualization and QC. P-wave velocity, S-wave velocity, and density were de-spiked, taking care that no lithology related spike was removed. Gamma-ray was used as the main lithology discriminator, whilst bit size and caliper were used to measure how reliable the measurements were at a given depth. Gaps with missing data or inconsistent data were disregarded.

Figure 3.3 represents the visualization of well 6507/11-8. It is zoomed on the target zone around Garn and Ile Formations. In the area around the shale that caps the Garn Formation, there is strong caving shown by the caliper, and density correction is over 0.15 g/cc. All that part of the well is disregarded. There is also strong caving in the Not Formation, the shale present between Garn and Ile is also well defined in the log. Caving is only affecting a segment within the Not Formation, density values are interpolated between unaffected zones within the same shale. Sonic measurement does not seem to be as affected by caving as the density measurements. The rest of the well is fairly stable and no other anomalies are present. Only QC and conditioning of well 6507/11-8 is shown here. All wells were QCed and conditioned using the same criteria.

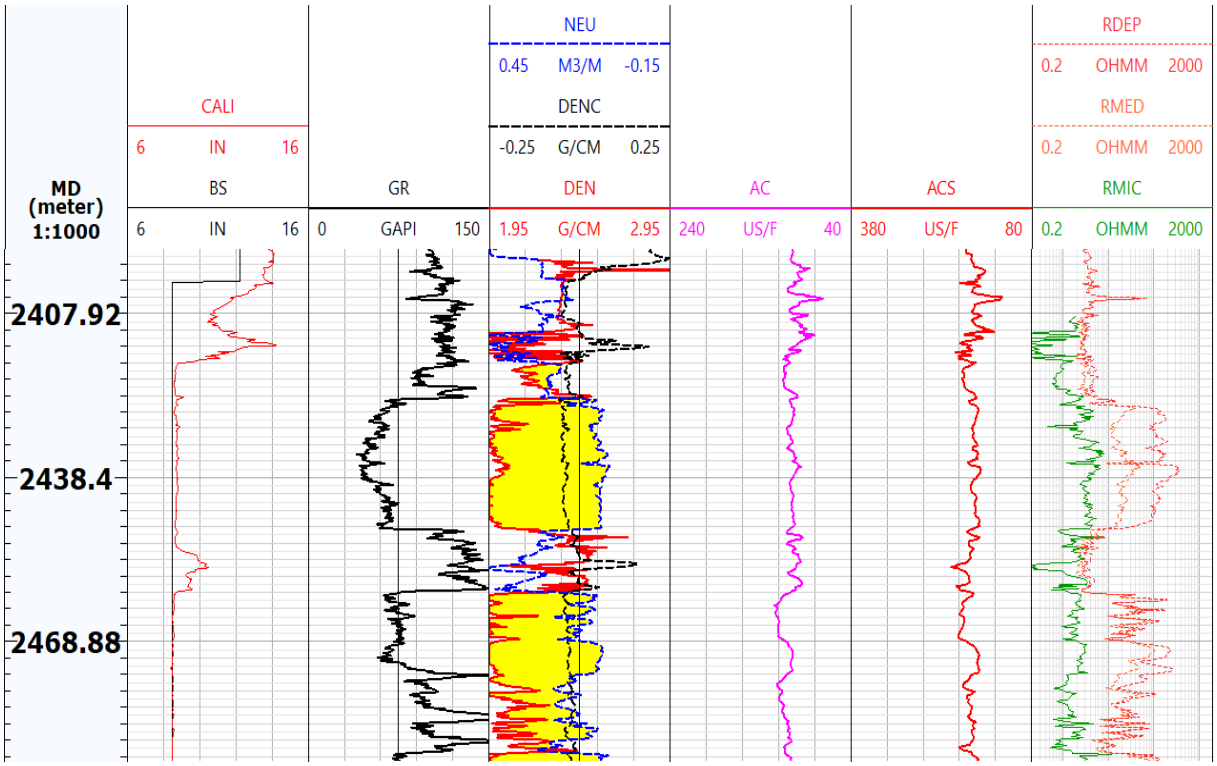


**Figure 3.3:** Well 6507/11-8 visualization and QC.

## 3.4 Gathers QC and stacking

There is confidence in the seismic quality due to knowledge and understanding of all the processes that have been applied to the data. Data loading is a QC process by itself since all byte locations have to be properly mapped and their contents must be accurate as well. There were no issues with the data loading and visualization.

Seismic data was partially stacked using only low angles of incidence (0 to 10 degrees) for well to seismic tie purposes and full stacked for conventional attribute calculations purposes. The amplitude spectrum for the full stack seismic is shown in figure 3.4. The seismic is known to be broadband and this is confirmed in the amplitude spectrum, where very low frequencies are in the data. This is relevant for the low-frequency model building process since the crossover of frequency does not need to be large. A low pass filter of 5 Hz pass and 10 Hz stop should be more than enough frequency crossover between seismic and model in this case.

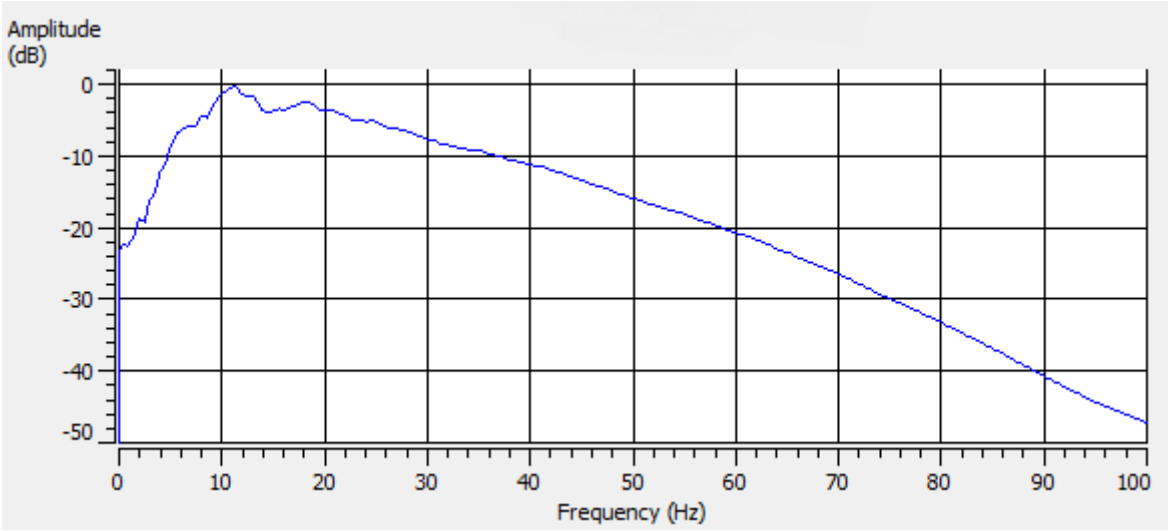


**Figure 3.4:** Seismic full stack amplitude spectrum

Interpreted horizons were loaded into the project at this stage as well. The correct placement of the interpreted horizons is a QC measure to ensure that the geometry is properly defined for the seismic and that the events are correct in time. Figure 3.5 shows Inline 2096 section for full stack data where interpreted top Kai, Base Tertiary, and Base Cretaceous Unconformity are shown. Horizons are important for the conventional LFM building method because they guide the interpolation under a stratigraphic framework.

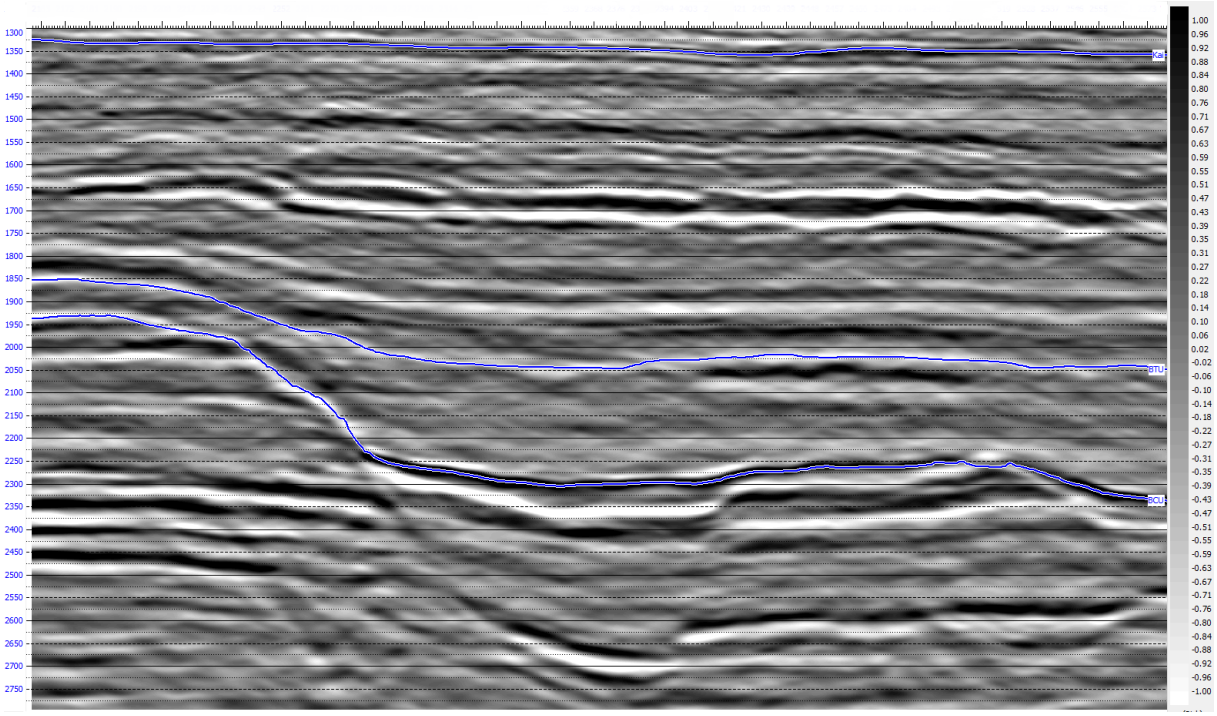

**Figure 3.5:** Full Stack seismic section for inline 2096 with interpreted horizons

## 3.5 Well-to-seismic tie

The well-to-seismic tie procedure can be outline with the following steps as described by White and Simm (2003):

1. Sonic log calibration.
2. Wavelet estimation
3. Synthetic seismogram from calibrated and conditioned logs
4. Match between observed seismic and modelled seismic.

The sonic log calibration is done by means of calculation a drift curve from the difference between the integrated sonic log times and the check-shot times. The calibration uses straight line segment between knee points. The knee points were chosen were relevant changes on the seismic log were present. The drift curve was then applied to the sonic log. An example for well 6507/11-2 is shown in figure 3.6. Well tops are available to aid knee location. It can be seen on the first panel that knees are picked at trend changes in the sonic log, which also coincides with lithology changes. The second panel is the residual drift for QC, notice that the residual drift is between ±2.5 ms. Third and last panel shows calibrated sonic log (blue) and uncalibrated sonic log (red).

Well 6507/11-11 had no check-shot available. A pseudo check-shot was created using the well report and interpreted horizons. The higher uncertainty of the pseudo check-shot can be seen in figure 3.7. No clear trend is visible on the drift curve. The residual drift log ranges from -35 ms to 25 ms. Sonic log calibration is not feasible is such context. Only sonic calibration for this particular well is performed just to calibrate the reference datum in the sonic log but no to calibrate the sonic log itself. It is assumed that the available sonic log is approximate to the calibrated sonic log, therefore no calibration is needed. This assumption may seem naive, but it is based on the small changes between calibrated and uncalibrated sonic logs on the other logs too. Figure 3.6 is again a good example of this fact.

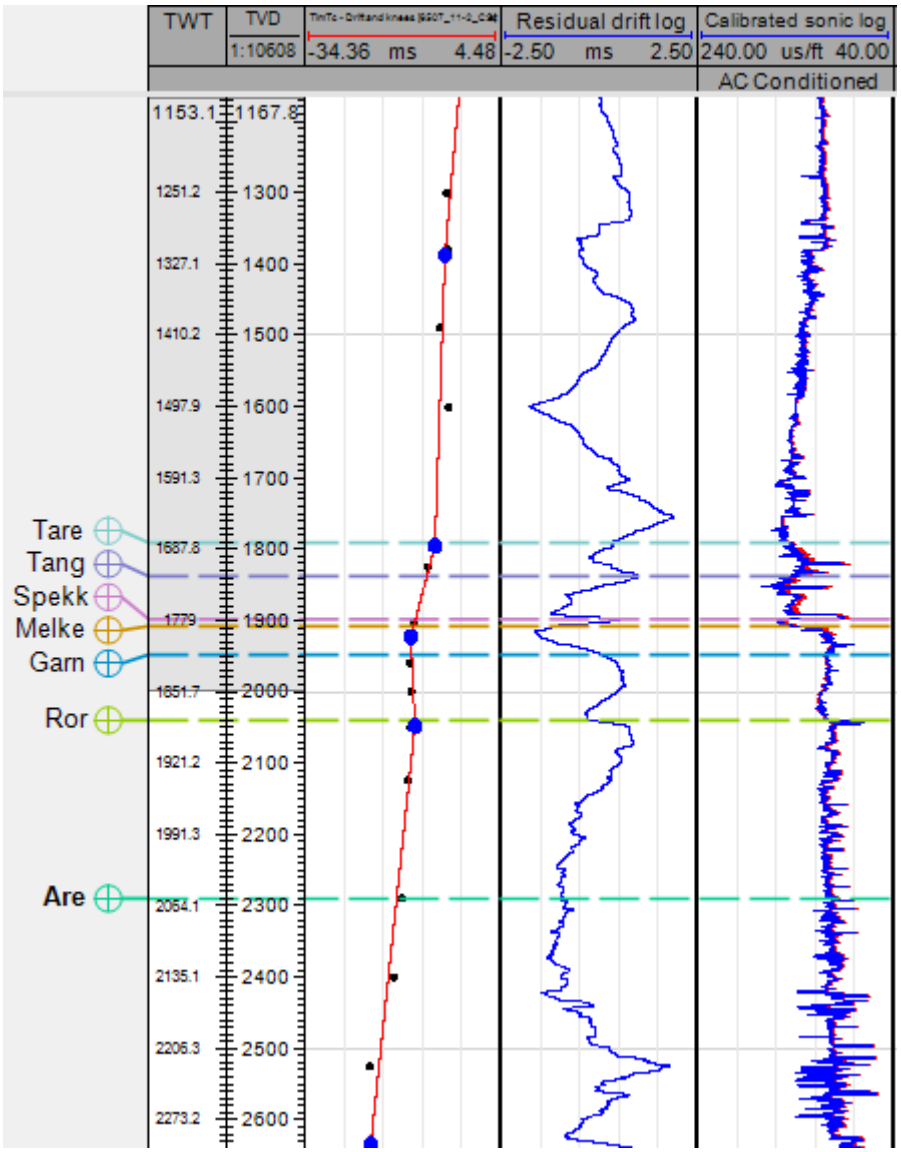


**Figure 3.6:** Sonic log calibration for well 6507/11-2. Left panel represents drift curve in red fitted by knee points in blue, black dots represent depths where check-shot measurements are available. Central panel is the residual drift after sonic calibration. Last panel represents the calibrated sonic log in blue and uncalibrated sonic log in red

Wavelet estimation was kept as simple as possible. Constant phase is assumed, then wavelets were estimated statistically at each well location. Zero-offset reflection coefficients were calculated from acoustic impedance derived from density and calibrated sonic logs. The zero-offset reflection coefficient series is then convolved with the estimated wavelet to generate the synthetic seismograms.

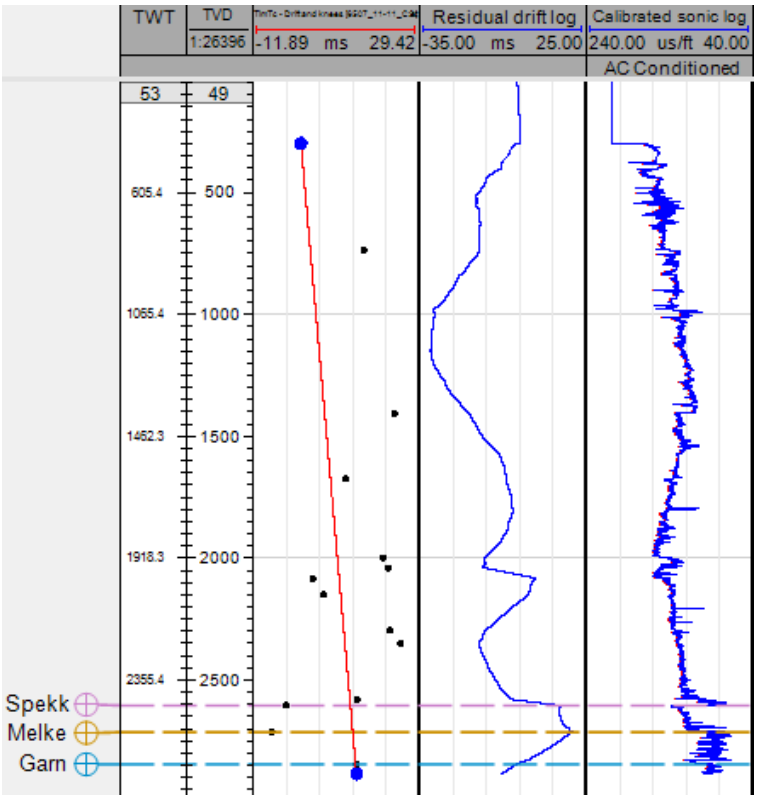


**Figure 3.7:** Sonic log calibration for well 6507/11-11. High uncertainty and high residual drift due to the lack of check-shot data

Synthetic seismogram and observed seismic match was kept as simple as possible as well. Only bulk shift was applied. Squeezing and stretching of the logs was avoided when possible. The match between modelled seismic and observed seismic proved to be excellent. Figure 3.8 shows the well-to-seismic match for well 6507/11-2, blue wiggles represent the synthetic seismogram, and red wiggles the composite trace from the seismic along the well path. This well is used as example for consistency, as the sonic log calibration for this well was also shown previously. As a QC measure, the cross-correlation coefficient between modelled seismic and observed seismic is 0.7.

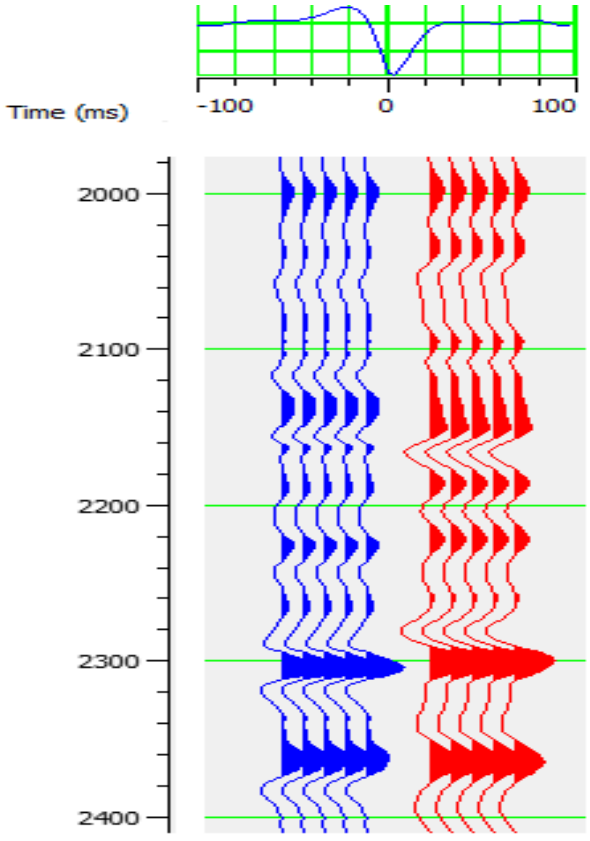


**Figure 3.8:** Well-to-seismic tie for well 6507/11-2. Modelled seismic in blue, observed seismic in red

Special care is taken for well 6507/11-11. This well is the only one that has no available check-shot data, and it is the main well to be used as blind test location as well. Due to the lack of check-shot data, well-to-seismic tie in this particular case required stretching of the well log. Figure 3.9 shows a detailed comparison between synthetic and observed seismic. Despite the lack of check-shot data, there is an excellent match between modelled seismic and observed seismic.

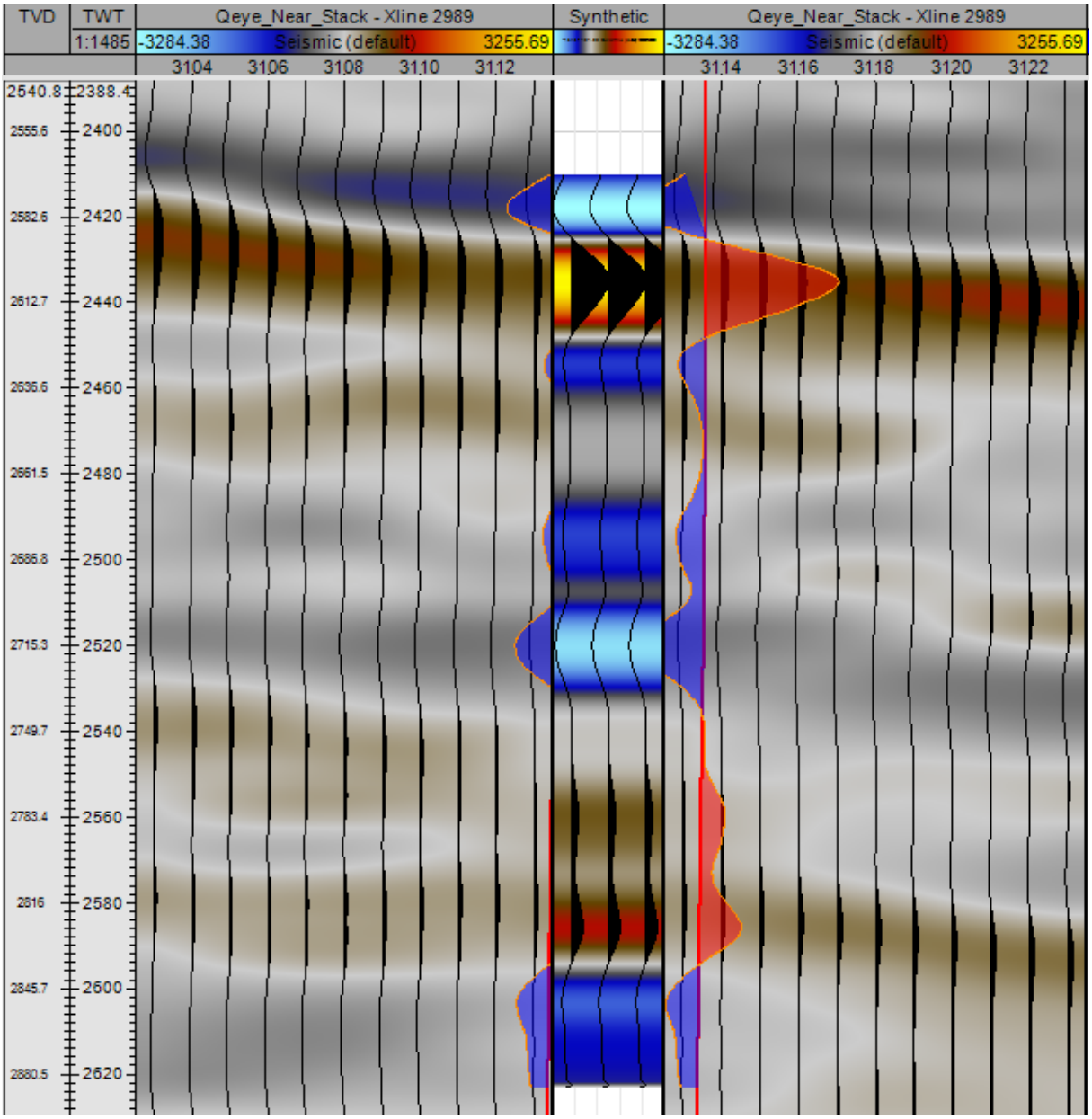


**Figure 3.9:** Well-to-seismic tie for well 6507/11-11. Excellent match between modelled (central panel) and observed seismic (lateral panels) despite lack of check-shot data

## 3.6 Seismic Attributes calculation

### 3.6.1 AVO attributes

One of the key elements of the proposed methodology is the consideration of prestack attributes as predicting attributes due to their well defined relation to elastic parameters. Two term Aki Richards AVO formulation to calculate Intercept and Gradient from available angle gathers was performed (equations 2.5). AVO attribute analysis is straightforward. Dropping the third term from equation 2.5 by limiting the angles to $\theta < 30°$, yields a linear equation in terms of $\sin^2\theta$. A linear regression of the amplitudes from angle gathers yields a linear equation of the form $A + B\sin^2\theta$, where $A$ happens to be Intercept, and $B$ the Gradient.

From calculated $A$ and $B$, other AVO attributes are calculated as well. $A \times sign(B)$, $A \times B$, $B \times sign(A)$, Scaled Poisson, and Scaled S-wave are derived from the initial analysis. The relation between elastic properties and these AVO attributes were explained in detail in the previous chapter.

### 3.6.2 Poststack seismic attributes

Only poststack attributes with suspected or known relationship with elastic parameter were derived. Different attribute classifications exist. In this case, the classification framework given by Taner et al. (2005) serves ideally to the purpose of this work. Under this classification, only physical attributes are considered. Physical attributes are those related to physical parameters of the subsurface that are relevant in reservoir characterization. For instance, AVO attributes are prestack physical attributes. Physical poststack attributes comprise amplitude envelope, integrated absolute amplitude, amplitude derivatives, instantaneous phase and frequency, dominant frequency, among others. These attributes are related to acoustic impedance contrast, major lithology changes, fluid effects, thin beds effects, etc. Even though physical attributes have a projected use in prediction of rock properties, not all of them are required or have a strong relationship with a particular rock property. It is part of the training optimization process to choose those more suited to be used as predictors. This process will be discussed in detail later in this chapter.

### 3.6.3 Relative Impedance volume

Acoustic impedance contrast between the rocks is closely related to the acoustic impedance of the rocks, therefore there is a well defined relation between relative impedance and absolute impedance and hence used as another attribute in the training data.

The calculation of relative acoustic impedance was carried out by Coloured Inversion, as described by Lancaster and Whitcombe (2000). It is based on the convolution of an operator wavelet with the seismic, to convert the seismic spectrum to that of the earth acoustic impedance spectrum from the well logs.

First, the average acoustic impedance spectrum from all well is calculated and a logarithmic function that fits the spectrum is estimated as shown in figure 3.10. It represents the earth acoustic impedance.

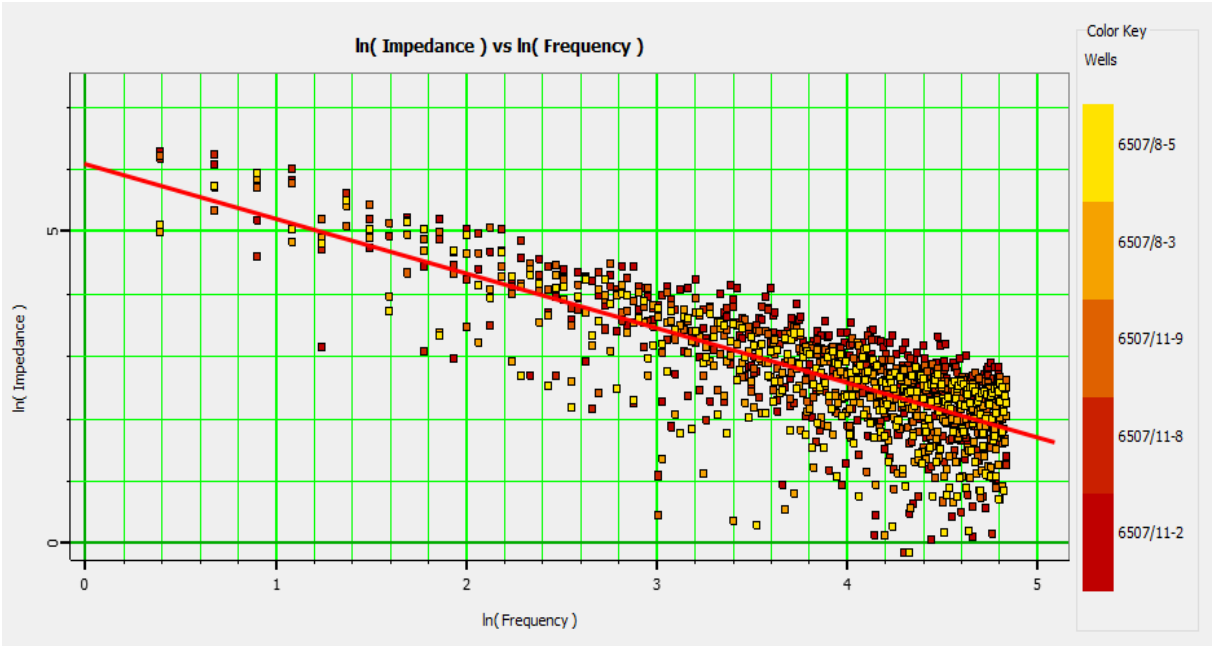


**Figure 3.10:** Acoustic impedance log spectrum and logarithmic function fit.

Then, the average seismic spectrum from a defined number of random seismic traces is calculated, to later obtain a difference spectrum by subtracting it to the modelled acoustic impedance spectrum. Figure 3.11 shows the average seismic spectrum in blue, whereas the modelled acoustic impedance spectrum is shown in red. The difference spectrum is shown in grey.

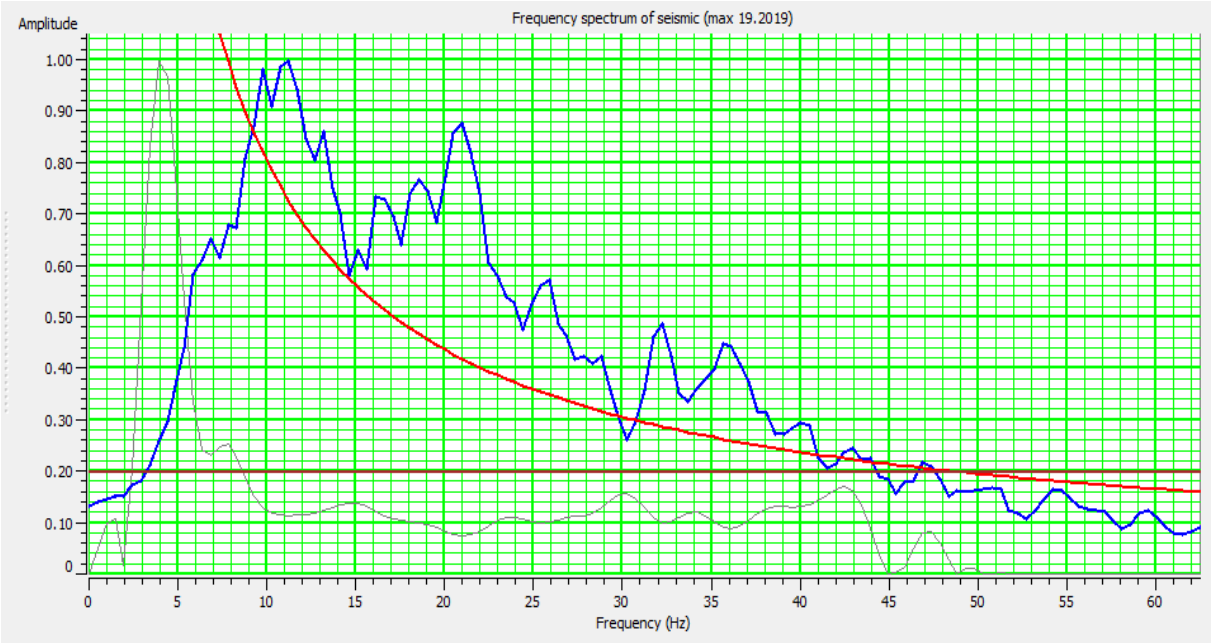


**Figure 3.11:** Average seismic spectrum (blue), modelled acoustic impedance spectrum (red), and difference spectrum (grey).

The difference spectrum is then converted into an operator by means of the inverse Fourier transform. The operator accounts for the difference between the calculated average seismic spectrum and the well derived spectrum. The final step is to convolve the operator with the seismic.

### 3.6.4 Conventional LFM and interval velocities

So far, all derived attributes are trend-less attributes or band-limited attributes. One of the issues to address in this work is not only how good a trend prediction can be using trend-less training data, but also using low-frequency information in the training data. The low-frequency content from well logs is used to build conventional low-frequency models constrained by interpreted horizons. On the other hand, RMS seismic velocities were available and converted to interval velocities. The frequency content from the available seismic velocities only covers the ultra-low frequencies as can be seen in figure 3.12, where the frequency content is below 2 Hz. This limited frequency content is one of the issues described by Sams and Carter (2017) when using seismic velocities for cokriging interpolation. Still, the very low-frequency information can aid to estimate trends away from well control.

Band-pass filtered logs (5 Hz pass - 10 Hz stop) were interpolated and guided by interpreted horizons using a single well. The single well selection criteria is defined in terms

of aim of the study. In this case, the aim is to better estimate away from well control, well 6507/11-11 was used as blind test location. The selected well had to capture all depth trends for all formations. Not all the log start at the same depth hence P-Impedance, S-Impedance, and $V_P/V_S$ do not necessarily logged the same formations for the same log. Given to this fact, the chosen representative well will depend on the target log also.

Using all available wells to build the conventional low-frequency model as an attribute was disregarded. If such a model is used to train a multivariate transform, there will be a perfect match at every well location because all wells were used to build the model and any other attribute will not improve the validation error in the best case scenario and it will worsen the estimates in most scenarios. It is equivalent to using the LFM alone and hence equivalent to the conventional method.

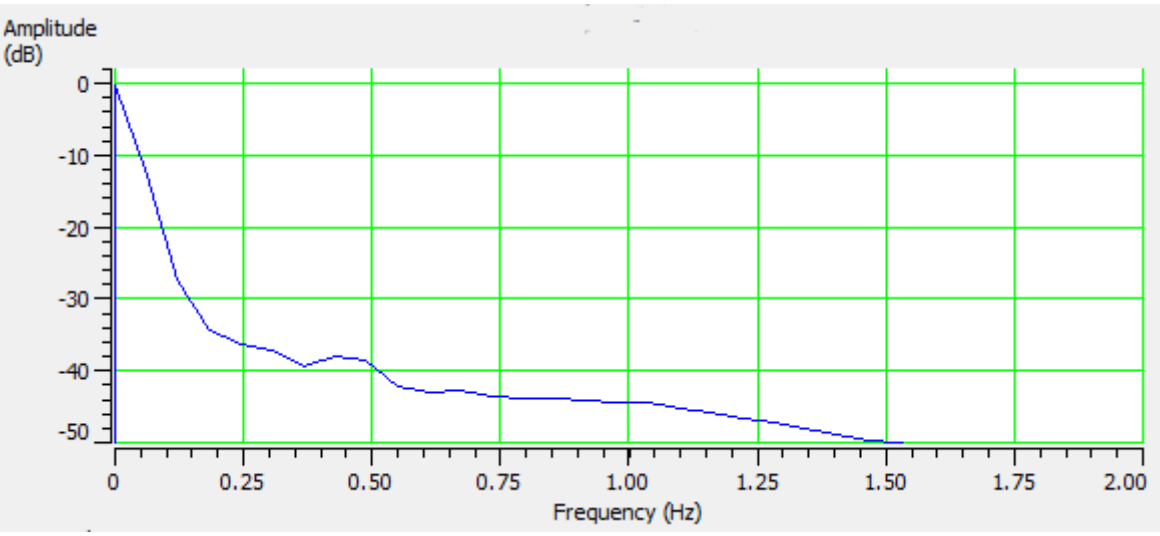


**Figure 3.12:** Seismic velocity amplitude spectrum

## 3.7 Multiattribute Analysis and training optimization

The first step is to set the target log and given that log samples do not necessarily coincide with the sample times of the seismic data, it is necessary to re-sample in order to avoid aliasing. There are two options, as stated by Banchs and Michelena (2002), at this point. The first option is to low-pass filter the log data and re-sample it to match the spectral content of the seismic data and the seismic time samples. The second option is to re-sample log data just to have uniform time samples but preserving its resolution, then it is necessary to up-sample the seismic data in order to match the log sample times.

The first option works perfectly for the objective of this work since we are aiming to es-

timate only the low-frequency content of the well-log information away from well control. The second option is preferable when the aim is to estimate absolute values, then it is convenient to preserve as much resolution power as possible. Both approaches are applied and the result differences discussed later in detail.

The next step is to select the training data to be used in the analysis. Target well logs, AVO volume attributes, poststack seismic, poststack seismic attributes, seismic velocities, relative impedance volume, and conventional low-frequency models are selected. A composite trace is calculated at each well location. This step is represented graphically in figure 3.13, note that not all available attributes are shown.

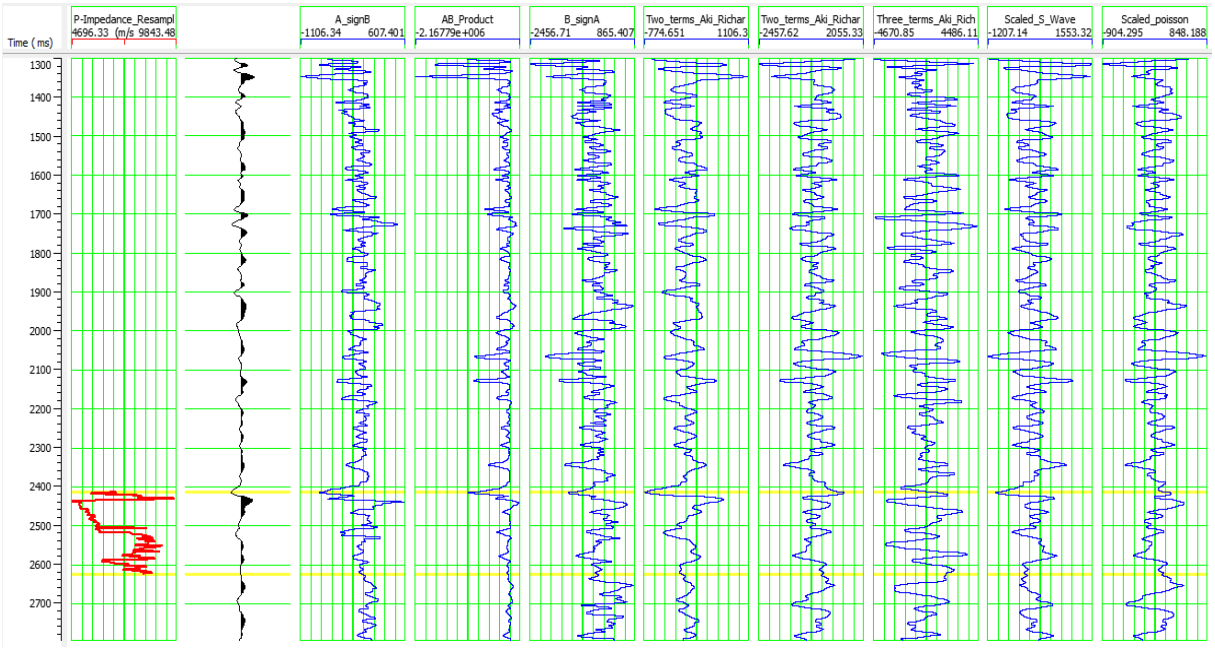


**Figure 3.13:** Input data for multiattribute analysis at well 6507/11-11 location. Target log in red, composite trace in black, and attributes in blue.

Setting the optimum analysis parameters is key. What attributes to use and size of the operator length are the main parameters to optimize. At first, what attributes relate best to a particular target log is unknown. A maximum number of attributes must be selected. In this case, a maximum of 10 attributes were selected and a maximum operator length of 9 times the sample rate is also selected. A high number of attributes and operator lengths at this point is better than a low number as over-training errors are usually significantly lower than under-training errors. The best 9 attributes are determined by step-wise regression. A ranked list of attributes will be determined for a particular operator length as shown in table 3.2. The training error and total validation error is also shown in the table. Attributes are

ranked from one to nine, being one of the attribute that best correlates with the target log, number two the second best, and similarly for the rest. The reason why a particular set of attributes is better than others is analyzed in the discussion chapter.

**Table 3.2:** Best nine attributes table. P-impedance is the target log. Training and validation errors are given in $(m/s) * (g/cc)$.

| Rank | Target | Attribute | Training error | Validation error |
|---|---|---|---|---|
| 1 | P-impedance | Conventional P-impendace LFM | 591 | 605 |
| 2 | P-impedance | Integrate | 547 | 568 |
| 3 | P-impedance | Scaled Poisson | 531 | 555 |
| 4 | P-impedance | Interval Velocity | 518 | 558 |
| 5 | P-impedance | Coloured Inversion | 515 | 556 |
| 6 | P-impedance | Cosine Instantaneous Phase | 510 | 551 |
| 7 | P-impedance | Filter 25/30-35/40 | 506 | 553 |
| 8 | P-impedance | Filter 35/40-45/50 | 504 | 566 |
| 9 | P-impedance | A * sign(B) | 501 | 568 |

The training error will always decrease as function of the number of attributes. Using a higher number of attributes is analogous to fitting a crossplot with an increasingly higher order polynomial but that might lead to over-training, fitting better at well control but worsening the estimates away from well control. The concept of cross-validation was explained in detail in the theoretical background and it yields the total validation error. The total validation error is the RMS average of the individual errors at individual blind locations. In contrast to the training error, validation error curves do not decrease monotonically. It exhibits a distinct minimum that it is assumed that the number of attributes at that point is optimum since it represents the limit between under-training and over-training. Then the best attributes and best operator length can be defined at this point. This is checked for the values in table 3.2 by plotting training error and validation error as function of the number of attributes (figure 3.14). For this particular case, it can be noted that the validation error is minimum at the 6th attribute. Going as far as nine attributes is as good as using only the two best attributes.

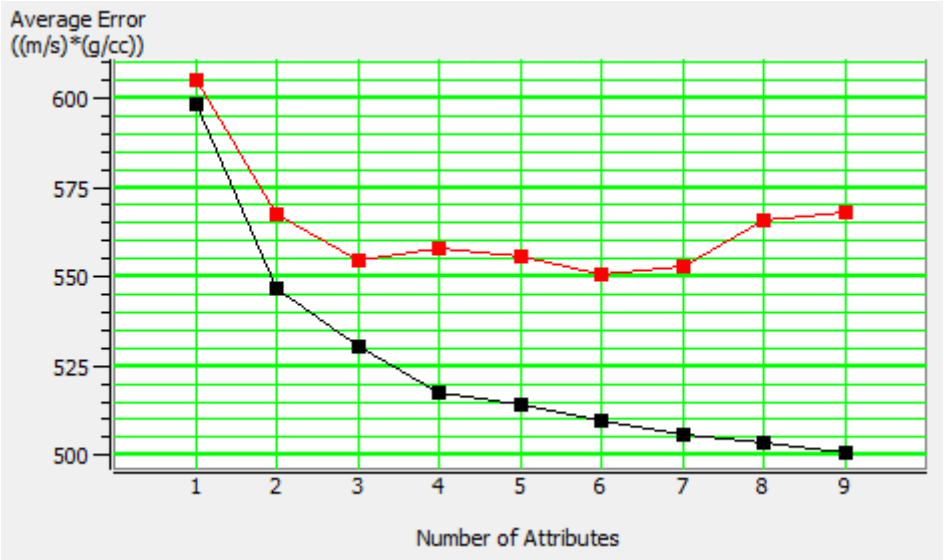


**Figure 3.14:** Training error (black) and Validation error (red) as a function of number of attributes. Data from table 3.2

Three Neural Networks algorithms are available: Probabilistic Neural Network (PNN), Multi-layer Feed Forward Network (MLFN), and Radial Basis Function (RBF). RBF are described as a rather simple kind of Neural Network and MLFN tend to fit the data too closely, leading easily to over-training. PNN is the most robust of the available Neural Network algorithms, with the only disadvantage of being more demanding computationally speaking, hence this work will focus on using PNN instead of RBF or MLFN. Given that Neural Networks operate best with stationary statistics, the PNN training is cascaded with the trend obtained from multi-linear regression using the attributes obtained with step-wise regression. Trained PNN is then validated using cross-validation.

## 3.8 Low-frequency estimation

Once the non-linear relation between the attributes and the target log have been defined and optimized, then this relation is applied to the whole volume of attributes yielding a volume of the target elastic parameter. The resulting volume is low-pass filtered and compared against the conventional method and the actual values at blind well location 6507/11-11. This well was never used at any moment during the work-flow, neither in the training data nor in the validation data in order to simulate a real case scenario of a true blind test for a proposed drilling location.

# Chapter 4

# Results

Results are divided by target log: Acoustic Impedance, Shear Impedance and $V_P/V_S$ ratio. At the same time, target logs are subdivided into two parts: non-filtered logs for absolutes estimates and low-pass filtered log. The reasoning to divide the target logs is to verify what the differences are, if any, between the two sampling approaches mentioned in the methodology chapter.

Two different input data-sets were used to train the multiattribute transforms. First data-set containing trendless data only and the second data-set containing low-frequency information from seismic velocities and conventional low-frequency model built using one well only. The well chosen to be the more representative of the regional P-impedance is 6507/11-2. The criteria for this selection is the target Group (Viking Group) at the blind test location (6507/11-11). Well 6507/11-2 has log samples almost through all the time window of interest, which is not the case for all other wells that only have samples focusing mainly in the Fangst Group. It may be the case other well would have been more representative if it had logged the Viking Group. For the Shear Impedance and $V_P/V_S$ ratio estimates, a different well was used since 6507/11-2 does not have S-wave velocity logged. Even for those wells that have S-wave logged, density measurements are not logged at same intervals. 6507/11-9 has S-wave velocity samples at much shallower depths than density, whereas for 6507/11-8 both start at the same depth. Density in both cases was only logged for the target area of the Fangst Group. What this implies is that it is not possible to choose a single well for conventional model building to estimate S-impedance, and that for $V_P/V_S$ that the single well can only be 6507/11-9.

## 4.1 Acoustic Impedance estimation

### 4.1.1 Absolute estimates

Table 4.1 summarizes the best five attributes calculated by means of step-wise regression to estimate absolute values of P-Impedance using trendless training data only. The single best attribute is Time which is equivalent to Depth. It is well known that acoustic impedance is directly related to burial depth as well as other elastic parameters are also related to depth, as S-impedance and $V_P/V_S$ ratio. AVO attributes Scaled Poisson and Intercept are third and fifth best attributes respectively. Instantaneous attributes Integrate and Second Derivative are second and fourth respectively.

Training and validation errors are also given in table 4.1. A plot of these errors as function of number of attributes is shown in figure 4.1. It can be seen that the optimum number of attributes is between the fourth and the fifth attribute listed in table 4.1, with an average validation error of 867 $(m/s) * (g/cc)$. The average validation error increases after the sixth attribute due to over-training. The average training error exhibits the expected monotonically decreasing feature.

**Table 4.1:** Best five attributes table for absolute P-impedance estimates using trendless training data only. Training and validation errors are given in $(m/s) * (g/cc)$.

| Rank | Target | Attribute | Training error | Validation error |
|---|---|---|---|---|
| 1 | P-impedance | Time | 871 | 890 |
| 2 | P-impedance | Integrate | 849 | 873 |
| 3 | P-impedance | Scaled Poisson | 843 | 868 |
| 4 | P-impedance | Second Derivative | 839 | 867 |
| 5 | P-impedance | AVO Intercept | 836 | 868 |

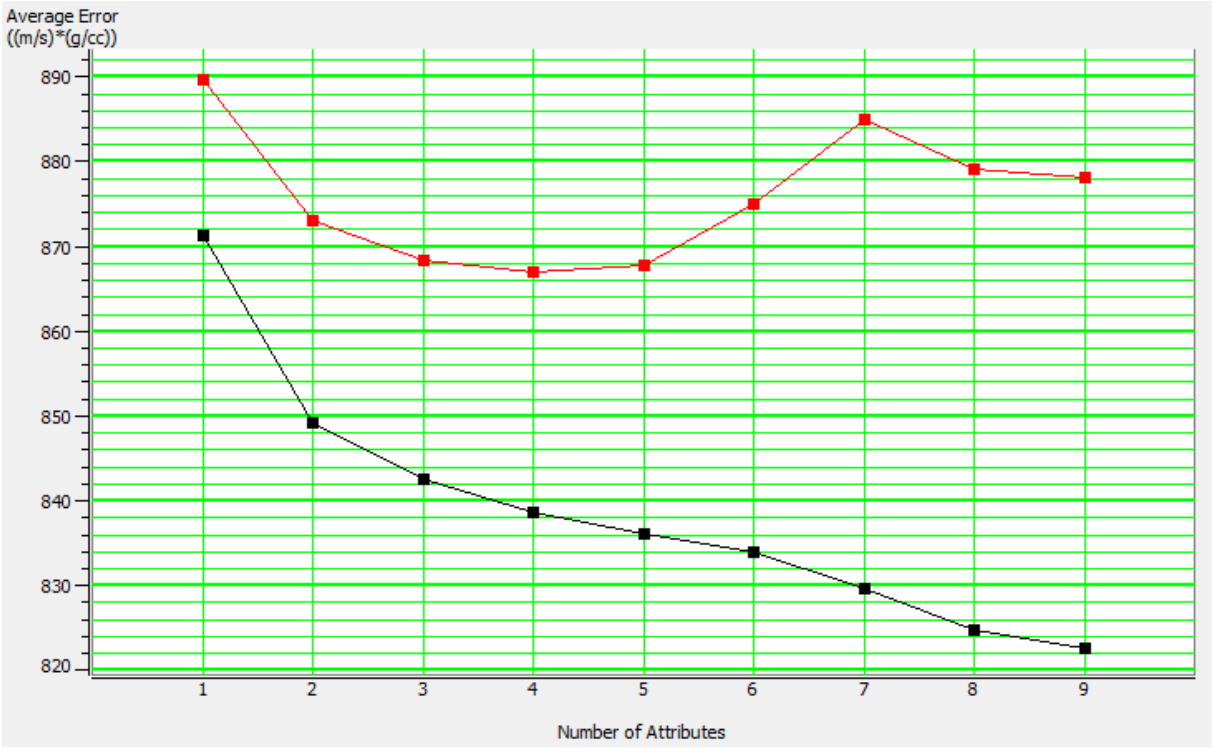


**Figure 4.1:** Training (black) and validation (red) average errors as function the number of attributes. Multiattribute transform trained with trendless data to estimate absolute P-Impedance values.

Table 4.2 summarizes the best five attributes calculated by means of step-wise regression to estimate absolute values of P-Impedance using trendless, interval velocity, and conventional low-frequency model built using a single well. Attributes containing low-frequency information are the first and second best attributes. AVO Scaled Poisson is fourth best. Integrate and Dominant Frequency are third and fifth respectively. Time is not longer in the list since interval velocity and conventional LFM contain the depth related information.

Training and validation errors are also given in table 4.2. A plot of these errors as function of number of attributes is shown in figure 4.2. It can be seen that the optimum number of attributes is again between the fourth and the fifth attribute listed in table 4.2, with an average validation error of 750 $(m/s) * (g/cc)$ which is more than 100 $(m/s) * (g/cc)$ lower than when using trendless data only. The average validation error does not increase significantly after the sixth attribute, therefore there are no signs of over-training within the first nine attributes.

**Table 4.2:** Best five attributes table for absolute P-impedance estimates using trendless training data, seismic velocities, and conventional low-frequency model built using one well only. Training and validation errors are given in $(m/s) * (g/cc)$.

| Rank | Target | Attribute | Training error | Validation error |
|---|---|---|---|---|
| 1 | P-Impedance | Interval Velocity | 804 | 830 |
| 2 | P-Impedance | Conventional LFM using one well | 631 | 764 |
| 3 | P-Impedance | Integrate | 621 | 752 |
| 4 | P-Impedance | Scaled Poisson | 613 | 747 |
| 5 | P-Impedance | Dominant Frequency | 611 | 748 |

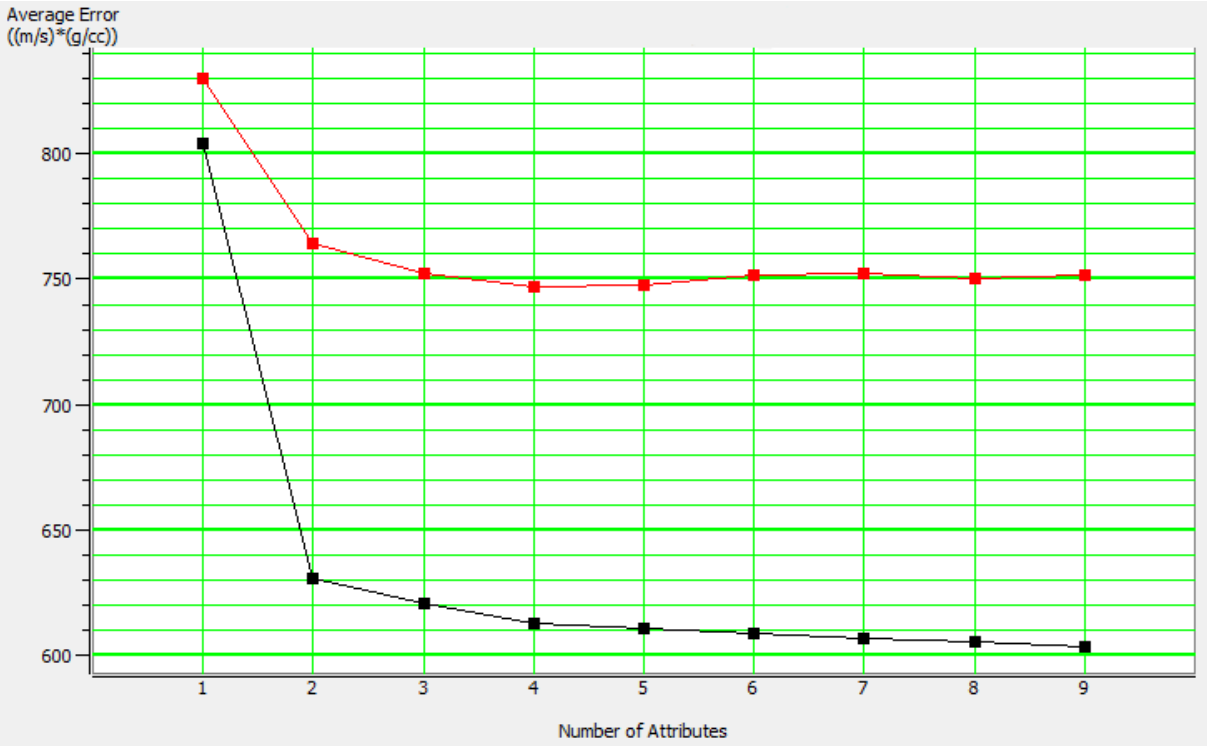


**Figure 4.2:** Training (black) and validation (red) average errors as function the number of attributes. Multiattribute transform trained with trendless data, seismic velocities, and conventional low-frequency model built using one well only to estimate absolute P-Impedance values.

### 4.1.2 Low-frequency estimates

Table 4.3 summarizes the best five attributes calculated by means of step-wise regression to estimate low-frequency values of P-Impedance using trendless training data only. The best attribute is Time, similarly as when estimating absolute values. The table is dominated by instantaneous poststack attributes (Average Frequency, Apparent Polarity, and Integrate). Only one AVO attribute is in the table.

Training and validation errors are also given in table 4.3. A plot of these errors as function of number of attributes is shown in figure 4.3. It can be seen that the optimum number of attributes is the single first attribute with an average validation error of 656 $(m/s) * (g/cc)$ which is more than 150 $(m/s) * (g/cc)$ lower than when estimating absolute values with the same input data . The average validation error increases after the first attribute due to over-training. On the other hand, the average training error exhibits the expected monotonically decreasing feature.

**Table 4.3:** Best five attributes table for low-frequency P-impedance estimates using trendless training data only. Training and validation errors are given in $(m/s) * (g/cc)$.

| Rank | Target | Attribute | Training error | Validation error |
|---|---|---|---|---|
| 1 | P-Impedance | Time | 644 | 656 |
| 2 | P-Impedance | Average Frequency | 639 | 710 |
| 3 | P-Impedance | Apparent Polarity | 636 | 704 |
| 4 | P-Impedance | Integrate | 633 | 702 |
| 5 | P-Impedance | Gradient * sign(Intercept) | 631 | 700 |

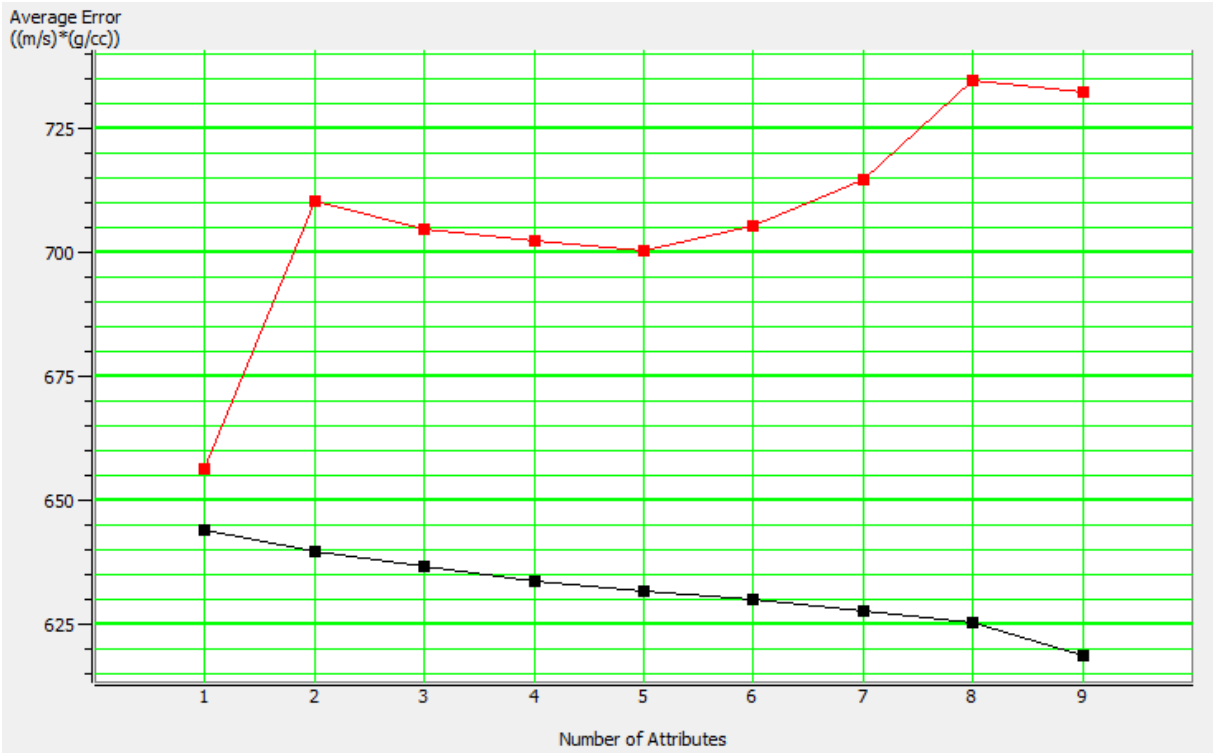


**Figure 4.3:** Training (black) and validation (red) average errors as function the number of attributes. Multiattribute transform trained with trendless data to estimate low-frequency P-Impedance values.

Table 4.4 summarizes the best seven attributes calculated by means of step-wise regres-

sion to estimate low-frequency values of P-Impedance using trendless, interval velocity, and conventional low-frequency model built using a single well. Attributes containing low-frequency information are the first and second best attributes. The rest of the attributes are mostly frequency-related instantaneous poststack attributes. No AVO attribute is in the table.

Training and validation errors are also given in table 4.4. A plot of these errors as function of number of attributes is shown in figure 4.4. So far, all other transforms had the fourth or the fifth attribute as the optimum number. In this case, the optimum number of attributes is seven, with an average validation error of 459 $(m/s) * (g/cc)$ which is the lowest average validation error for P-Impedance estimates.

**Table 4.4:** Best seven attributes table for low-frequency P-impedance estimates using trendless training data, seismic velocities, and conventional low-frequency model built using one well only. Training and validation errors are given in $(m/s) * (g/cc)$.

| Rank | Target | Attribute | Training error | Validation error |
|---|---|---|---|---|
| 1 | P-Impedance | Interval Velocity | 565 | 604 |
| 2 | P-Impedance | Conventional low-frequency model | 394 | 572 |
| 3 | P-Impedance | Average Frequency | 357 | 533 |
| 4 | P-Impedance | Integrated Absolute Amplitude | 317 | 522 |
| 5 | P-Impedance | Dominant Frequency | 300 | 482 |
| 6 | P-Impedance | Apparent Polarity | 291 | 467 |
| 7 | P-Impedance | Amplitude Weighted Frequency | 279 | 459 |

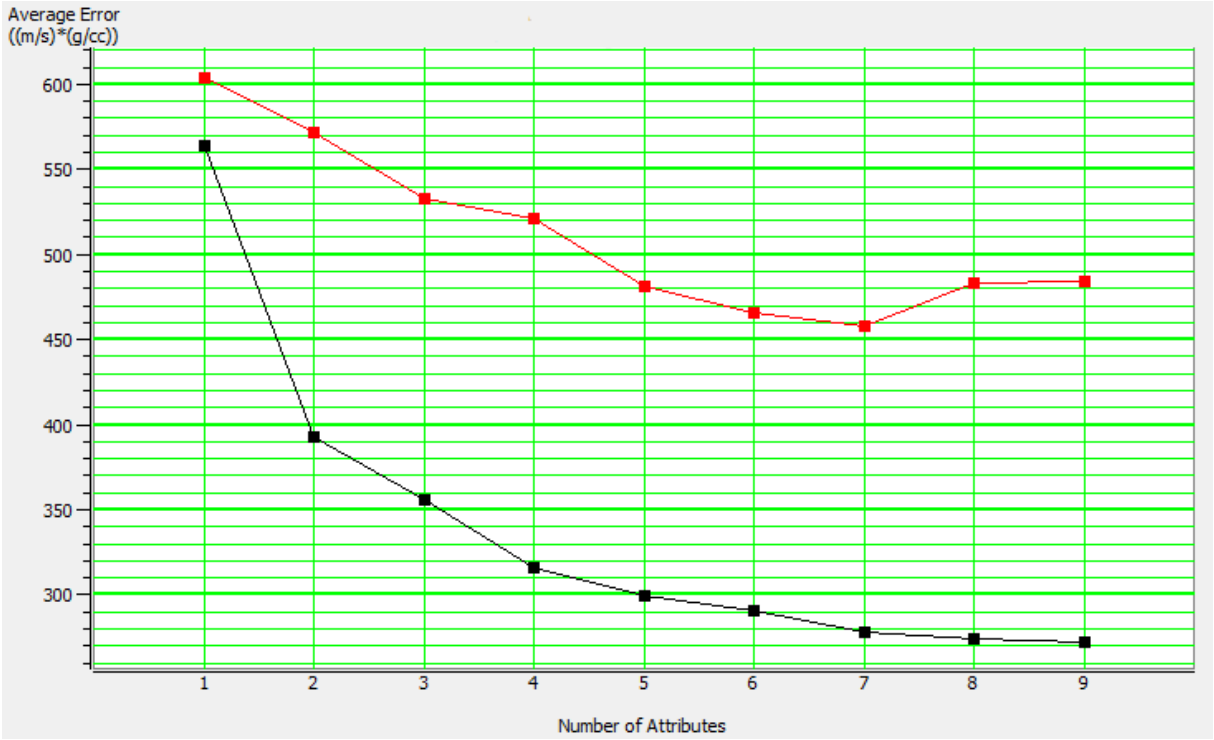


**Figure 4.4:** Training (black) and validation (red) average errors as function the number of attributes. Multiattribute transform trained with trendless data, seismic velocities, and conventional low-frequency model built using one well only to estimate low-frequency P-Impedance values.

## 4.2 Shear Impedance estimation

### 4.2.1 Absolute estimates

Table 4.5 summarizes the best ten attributes calculated by means of step-wise regression to estimate absolute values of S-Impedance using trendless data only. Time is the single best attribute as for P-impedance under the same context. Coloured Inversion is the fifth best attribute. AVO attributes such as Scaled Poisson, Intercept, and Scaled S-wave are in the list in the third, sixth, and eighth position respectively.

Training and validation errors are also given in table 4.5. A plot of these errors as function of number of attributes is shown in figure 4.5. It shows that the minimum of the function is at the 10th best attribute, then it increases due to over-training. The average validation error is 306 $(m/s) * (g/cc)$ at the optimum attribute number. The lowest average validation error for P-impedance estimates was 459 $(m/s) * (g/cc)$ as reference.

**Table 4.5:** Best ten attributes table for absolute S-impedance estimates using trendless training data only. Training and validation errors are given in $(m/s) * (g/cc)$.

| Rank | Target | Attribute | Training error | Validation error |
|---|---|---|---|---|
| 1 | S-impedance | Time | 334 | 357 |
| 2 | S-impedance | Amplitude Envelope | 312 | 399 |
| 3 | S-impedance | Scaled Poisson | 299 | 350 |
| 4 | S-impedance | Average Frequency | 292 | 417 |
| 5 | S-impedance | Coloured Inversion | 285 | 341 |
| 6 | S-impedance | AVO Intercept | 279 | 330 |
| 7 | S-impedance | Derivative | 272 | 321 |
| 8 | S-impedance | Scaled S-wave | 269 | 314 |
| 9 | S-impedance | Apparent Polarity | 267 | 306 |
| 10 | S-impedance | Intercept * Gradient | 265 | 310 |

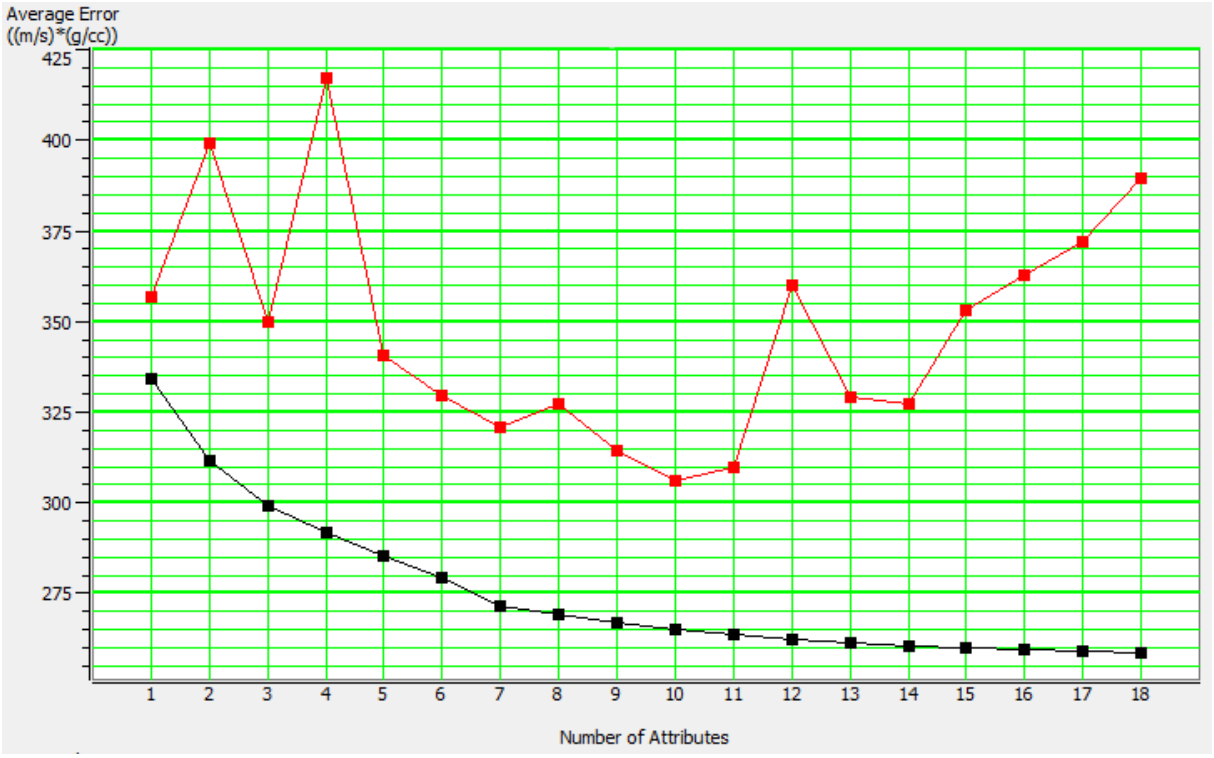


**Figure 4.5:** Training (black) and validation (red) average errors as function the number of attributes. Multiattribute transform trained with trendless data to estimate absolute S-Impedance values.

### 4.2.2 Low-frequency estimates

Table 4.6 summarizes the best four attributes calculated by means of step-wise regression to estimate low-frequency values of S-Impedance using trendless data only. Time is the single best attribute. Dominant Frequency, Apparent Polarity, and Integrate are the second, third and fourth best attributes respectively.

Training and validation errors are also given in table 4.6. A plot of these errors as function of number of attributes is shown in figure 4.6. As it can be noted, the single best attribute yields the lowest average validation error of 181 $(m/s) * (g/cc)$, then the average validation error increases drastically due to over-training. The average training error exhibits the expected monotonically decreasing feature.

**Table 4.6:** Best four attributes table for low-frequency S-impedance estimates using trendless training data only. Training and validation errors are given in $(m/s) * (g/cc)$.

| Rank | Target | Attribute | Training error | Validation error |
|---|---|---|---|---|
| 1 | S-Impedance | Time | 115 | 181 |
| 2 | S-Impedance | Dominant Frequency | 102 | 1326 |
| 3 | S-Impedance | Apparent Polarity | 92 | 1574 |
| 4 | S-Impedance | Integrate | 79 | 1151 |

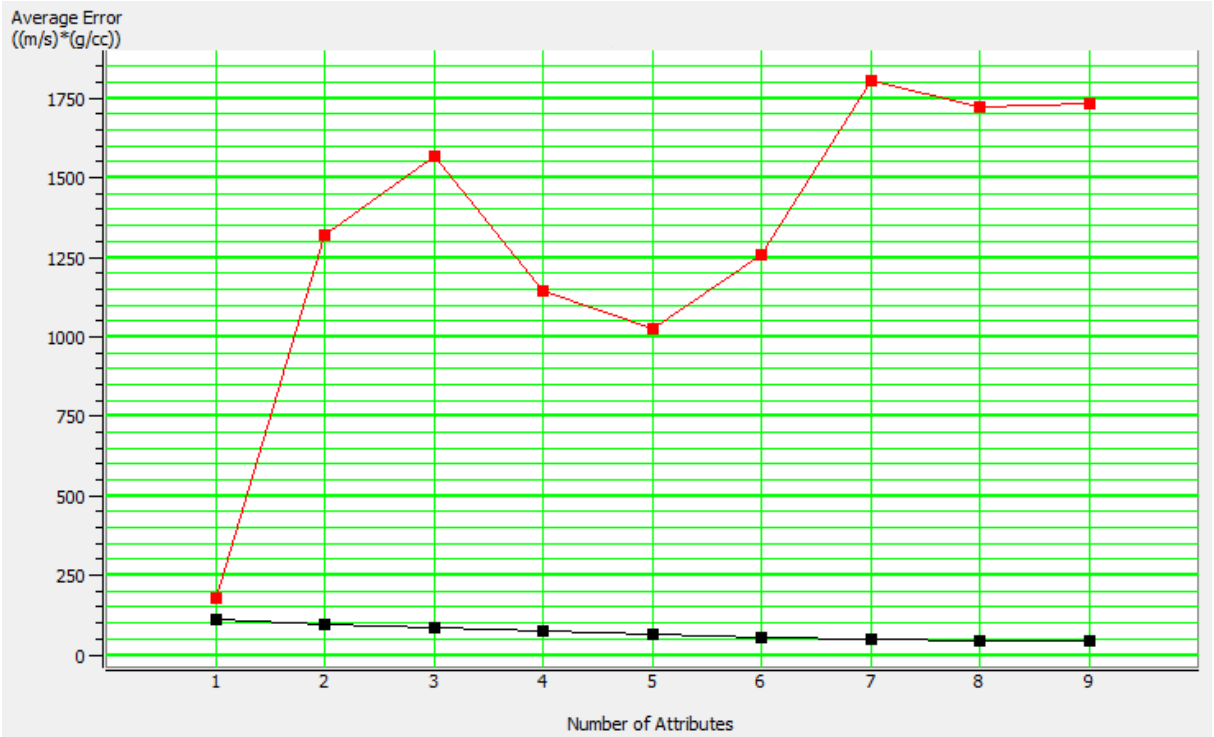


**Figure 4.6:** Training (black) and validation (red) average errors as function the number of attributes. Multiattribute transform trained with trendless data to estimate low-frequency S-Impedance values.

## 4.3 Vp/Vs ratio estimation

### 4.3.1 Absolute estimates

Table 4.7 summarizes the best four attributes calculated by means of step-wise regression to estimate absolute values of $V_P / V_S$ using trendless training data only. The single best attribute is Time, which is also the case when estimating absolute P-Impedance and S-Impedance using trendless data only. Second and third best attributes are Dominant Frequency and Amplitude Envelope.

Training and validation errors are also given in table 4.7. A plot of these errors as function of number of attributes is shown in figure 4.7. It can be seen that the optimum number of attributes at the second best attribute with an average validation error of 0.30. The average validation error increases after the second attribute due to over-training. The average training error exhibits the expected monotonically decreasing feature.

**Table 4.7:** Best four attributes table for absolute $V_P/V_S$ estimates using trendless training data only. Training and validation errors are given in $(m/s) * (g/cc)$.

| Rank | Target | Attribute | Training error | Validation error |
|---|---|---|---|---|
| 1 | $V_P/V_S$ | Time | 0.18 | 0.31 |
| 2 | $V_P/V_S$ | Dominant Frequency | 0.17 | 0.30 |
| 3 | $V_P/V_S$ | Amplitude Envelope | 0.16 | 0.32 |
| 4 | $V_P/V_S$ | Intercept * sign(Gradient) | 0.16 | 0.32 |

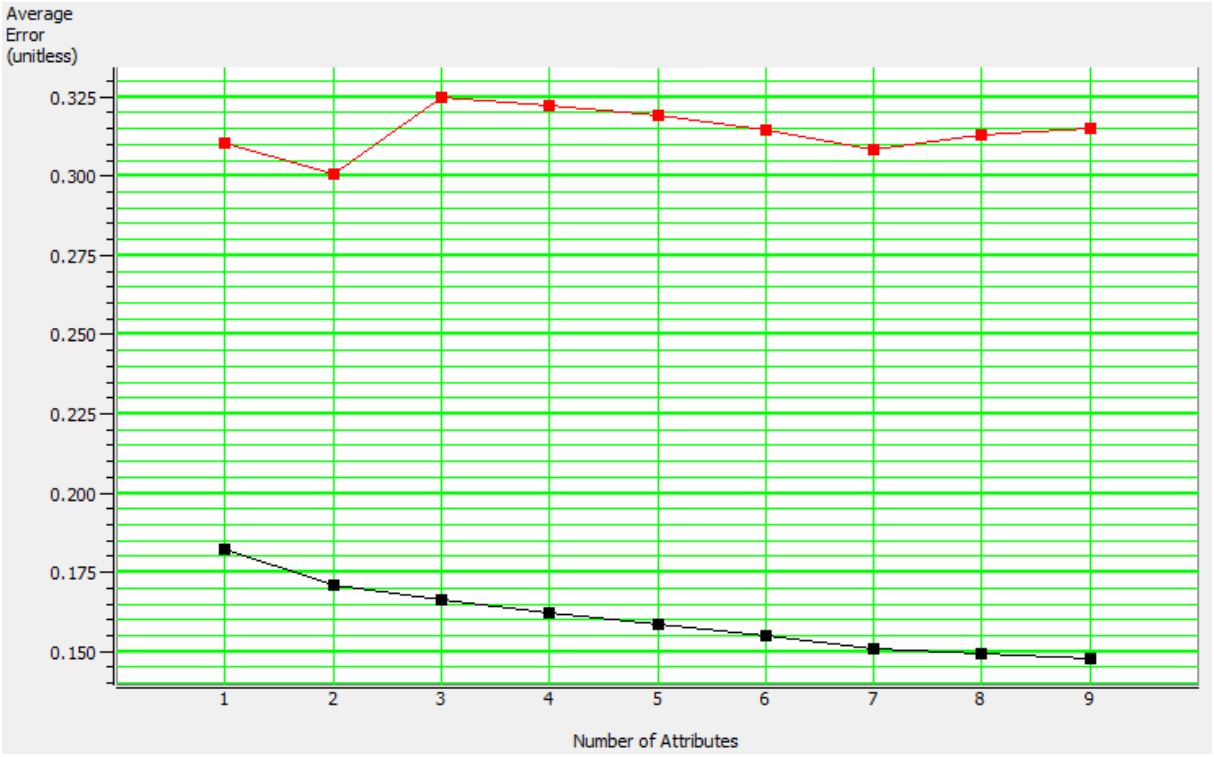


**Figure 4.7:** Training (black) and validation (red) average errors as function the number of attributes. Multiattribute transform trained with trendless data to estimate absolute $V_P/V_S$ values.

Table 4.8 summarizes the best ten attributes calculated by means of step-wise regression to estimate absolute values of $V_P/V_S$ using trendless and conventional low-frequency model built using a single well. The conventional LFM is the single best attribute, followed by Time and Dominant Frequency respectively. Different AVO attributes are also present in the table as well as Coloured Inversion as the seventh best attribute.

Training and validation errors are also given in table 4.8. A plot of these errors as function of number of attributes is shown in figure 4.8. It can be seen that the optimum number of attributes is ten attributes, as listed in table 4.8 with an average validation error of 0.194 which is around 0.1 lower than when using trendless data only. The average validation error

increases after the tenth attribute due to over-training. The average training error exhibits the expected monotonically decreasing feature.

**Table 4.8:** Best ten attributes table for absolute $V_P/V_S$ estimates using trendless training data and conventional low-frequency model built using one well only. Training and validation errors are given in $(m/s)*(g/cc)$.

| Rank | Target | Attribute | Training error | Validation error |
|---|---|---|---|---|
| 1 | $V_P/V_S$ | Conventional LFM using one well | 0.122 | 0.245 |
| 2 | $V_P/V_S$ | Time | 0.093 | 0.235 |
| 3 | $V_P/V_S$ | Dominant Frequency | 0.088 | 0.233 |
| 4 | $V_P/V_S$ | Scaled S-wave | 0.084 | 0.216 |
| 5 | $V_P/V_S$ | Intercept * sign(Gradient) | 0.081 | 0.222 |
| 6 | $V_P/V_S$ | Gradient * sign(Intercept) | 0.079 | 0.205 |
| 7 | $V_P/V_S$ | Coloured Inversion | 0.078 | 0.197 |
| 8 | $V_P/V_S$ | Apparent Polarity | 0.077 | 0.199 |
| 9 | $V_P/V_S$ | Amplitude Envelope | 0.075 | 0.194 |
| 10 | $V_P/V_S$ | Intercept * Gradient | 0.074 | 0.194 |

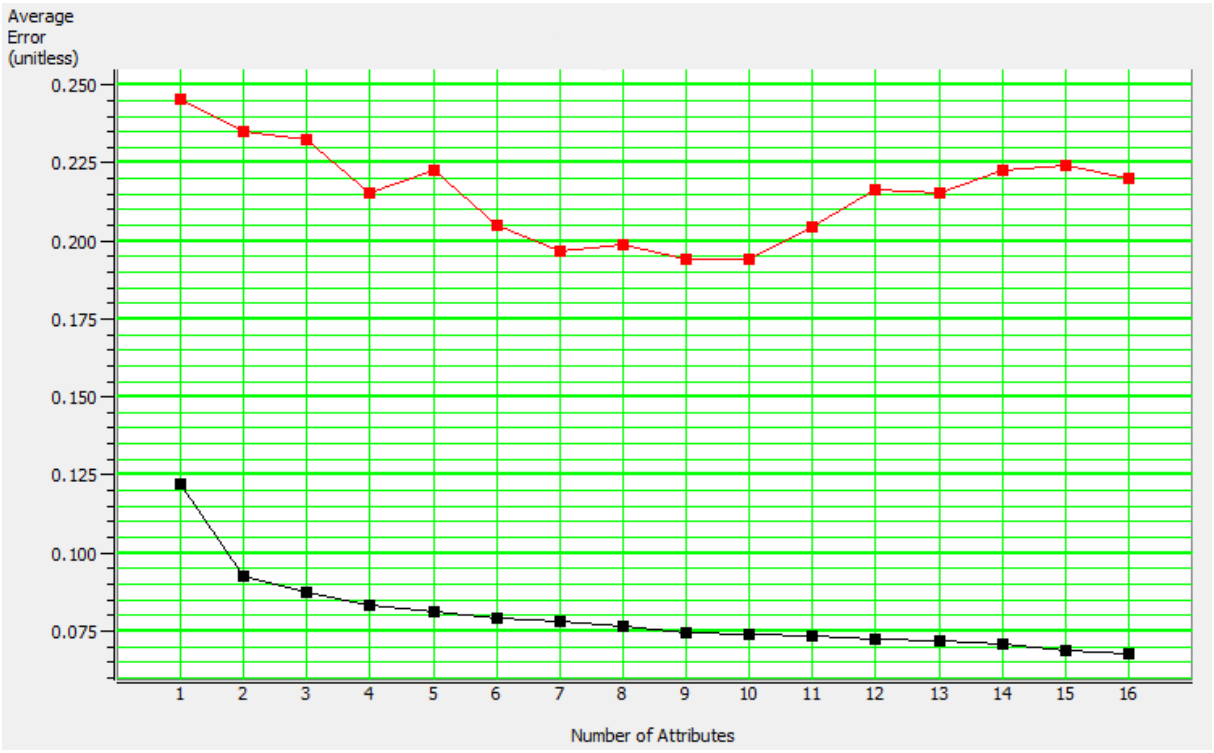


**Figure 4.8:** Training (black) and validation (red) average errors as function the number of attributes. Multiattribute transform trained with trendless data and conventional low-frequency model built using one well only to estimate absolute $V_P/V_S$ values.

### 4.3.2 Low-frequency estimates

Table 4.9 summarizes the best four attributes calculated by means of step-wise regression to estimate low-frequency values of $V_P/V_S$ using trendless training data only. The single best attribute is Average Frequency, the second is Dominant Frequency and the third is Integrated Absolute Amplitude. The table is dominated by instantaneous poststack attributes.

Training and validation errors are also given in table 4.9. A plot of these errors as function of number of attributes is shown in figure 4.9. It can be seen that the optimum number of attributes is three with an average validation error of 0.23 which is 0.07 lower than when estimating absolute values with the same input data . The average validation error increases significantly after the third attribute due to strong over-training. On the other hand, the average training error exhibits the expected monotonically decreasing feature.

**Table 4.9:** Best four attributes table for low-frequency $V_P/V_S$ estimates using trendless training data only. Training and validation errors are given in $(m/s) * (g/cc)$.

| Rank | Target | Attribute | Training error | Validation error |
|---|---|---|---|---|
| 1 | $V_P/V_S$ | Average Frequency | 0.158 | 0.29 |
| 2 | $V_P/V_S$ | Dominant Frequency | 0.125 | 0.28 |
| 3 | $V_P/V_S$ | Integrated Absolute Amplitude | 0.120 | 0.23 |
| 4 | $V_P/V_S$ | Time | 0.116 | 0.52 |

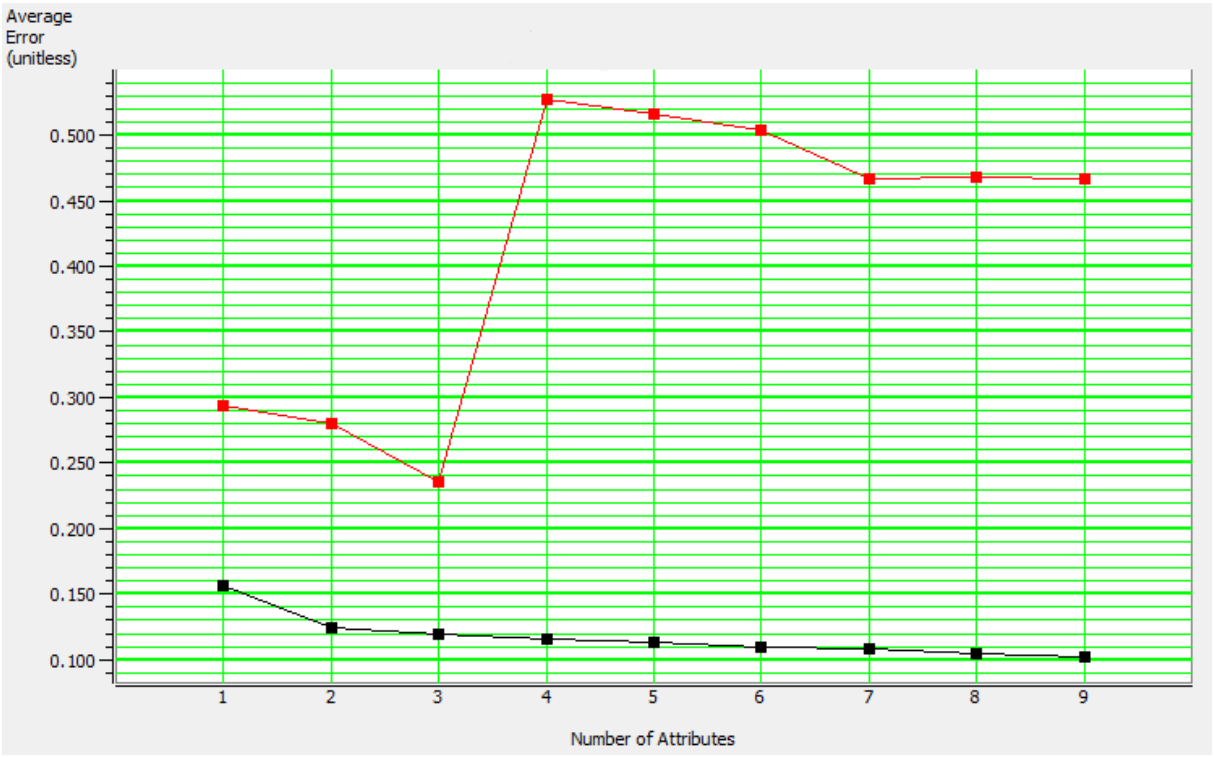


**Figure 4.9:** Training (black) and validation (red) average errors as function the number of attributes. Multiattribute transform trained with trendless data to estimate low-frequency $V_P/V_S$ values.

Table 4.10 summarizes the optimum attributes calculated by means of step-wise regression to estimate low-frequency values of $V_P/V_S$ using trendless and the conventional low-frequency model built using a single well. The best single attribute is the conventional low-frequency model, whereas Average Frequency, Time and Dominant frequency are second, third and fourth best attributes respectively. Coloured Inversion is the tenth best attribute.

Training and validation errors are also given in table 4.10. A plot of these errors as function of number of attributes is shown in figure 4.10. Similarly as for absolute estimates using the same input, the optimum number of attributes is large compared to using trendless data. It can be seen that the optimum attribute number is twelve. The average validation error at this point is 0.171 which is the absolute lowest average validation error for $V_P/V_S$ estimates. Yet again, the average training error exhibits the expected monotonically decreasing feature.

**Table 4.10:** Best twelve attributes table for low-frequency $V_P/V_S$ estimates using trendless training data and conventional low-frequency model built using one well only. Training and validation errors are given in $(m/s) * (g/cc)$.

| Rank | Target | Attribute | Training error | Validation error |
|---|---|---|---|---|
| 1 | $V_P/V_S$ | Conventional LFM using one well | 0.105 | 0.477 |
| 2 | $V_P/V_S$ | Average Frequency | 0.663 | 0.352 |
| 3 | $V_P/V_S$ | Time | 0.057 | 0.501 |
| 4 | $V_P/V_S$ | Dominant Frequency | 0.050 | 0.467 |
| 5 | $V_P/V_S$ | Integrated Absolute Amplitude | 0.041 | 0.307 |
| 6 | $V_P/V_S$ | Gradient * sign(Intercept) | 0.039 | 0.282 |
| 7 | $V_P/V_S$ | Intercept * sign(Gradient) | 0.036 | 0.256 |
| 8 | $V_P/V_S$ | Apparent Polarity | 0.034 | 0.206 |
| 9 | $V_P/V_S$ | Integrate | 0.032 | 0.189 |
| 10 | $V_P/V_S$ | Coloured Inversion | 0.030 | 0.183 |
| 11 | $V_P/V_S$ | AVO Gradient | 0.028 | 0.175 |
| 12 | $V_P/V_S$ | Intercept * Gradient | 0.027 | 0.171 |

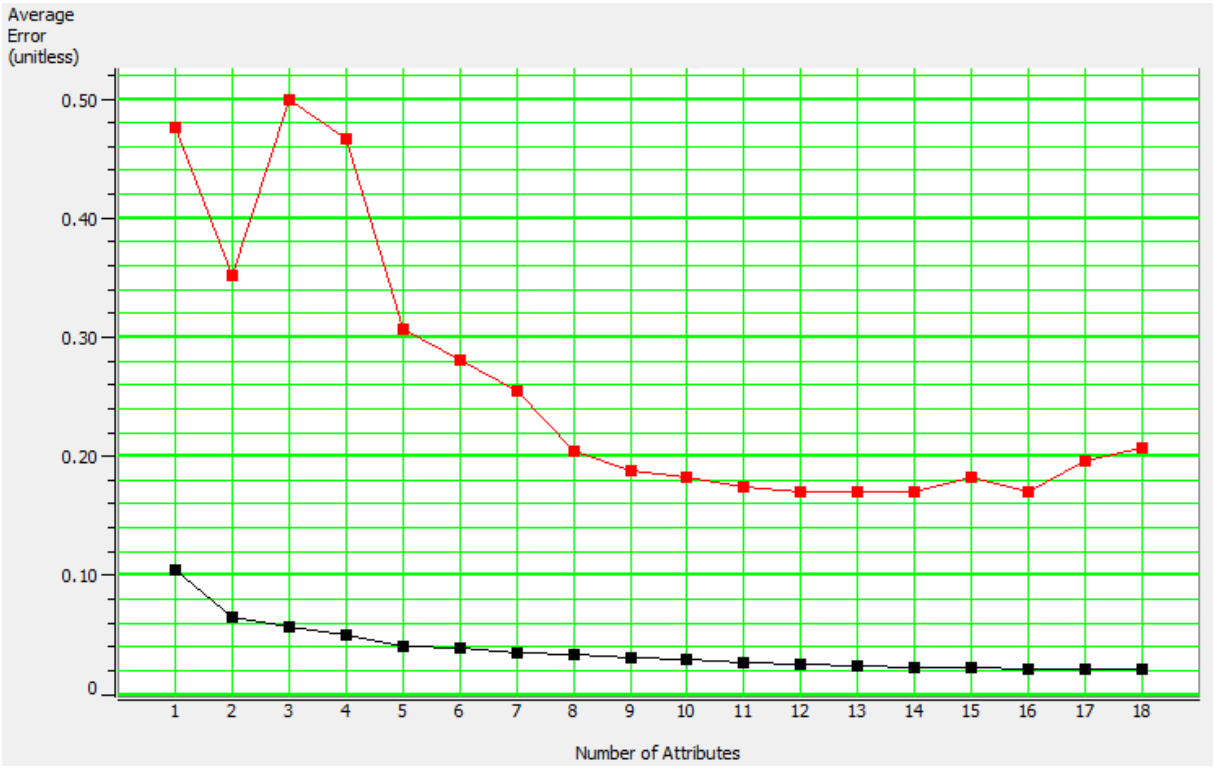


**Figure 4.10:** Training (black) and validation (red) average errors as function the number of attributes. Multiattribute transform trained with trendless data and conventional low-frequency model built using one well only to estimate low-frequency $V_P/V_S$ values.

# Chapter 5

# Discussion

From the multiattribute transforms training for P-impedance, it can be noted that interval velocity relates better than a conventional model low-frequency model built using a representative single well. Even though seismic derived velocities are within the very-low frequencies, they represent the seismic attribute that is closest to true interval velocity. Therefore, if more accurate and high-resolution compressional velocities could be derived from the existing seismic, better estimates of acoustic impedance could be derived as well. Full-waveform inversion has the potential to produce accurate velocity models at a resolution of up to 30 Hz (Mancini et al., 2016). This resolution cannot be matched by neither automated high-density velocity nor travel time tomography. That means that velocities derived using Full-waveform inversion can greatly improve P-Impedance estimates. This must be one of the main considerations for future studies that aim to estimate robust P-Impedance low-frequency models.

The second fact that stands out is that instantaneous frequency-related poststack attributes (e.g. Average Frequency, Dominant Frequency, and Amplitude Weighted Frequency) relate better than AVO attributes, particularly when estimating the low-frequency content directly of P-Impedance. This means that the actual frequency content from the seismic can drive the transforms. This might be related to the fact that the seismic used for this study is broadband seismic. It is not expected that conventional seismic can drive low-frequency information in a similar way. Still, AVO attributes contribute to the multiattribute transform.

The low-frequency content actually comes from the facies distribution, said in other words,it comes from the Net-to-Gross. It can be seen as the "average" of interbedded sequences. The low-frequency model is then controlled by the Net-to-Gross at seismic scale. The purpose of a seismic inversion can be to determine the Net-to-Gross of a given reservoir

because the Net-to-Gross is unknown away from well control. Here is where AVO attributes are valuable because they contain Net-to-Gross information that is required to built more robust low-frequency models (Stovas et al., 2005).

Time is the single best attribute when no other attribute containing low-frequency information is used. All elastic parameters are directly related to depth. As there is a well established Depth-Time relationship, it is expected that Time is the single best attribute in such context. This is the case not only for P-Impedance but also for S-Impedance and $V_P/V_S$ when using trendless data only to train the transforms.

Figure 5.1 shows all low-frequency estimates for P-Impedance, $V_P/V_S$, and S-Impedance after applying the trained transforms shown in the results chapter. It can be seen that using trendless data generates estimates with low-frequency content. The frequency content is very limited when using trendless input data in the transforms as it can be seen in the figure, normally below 2 Hz. In a real case scenario, the multiattribute training with the lowest average validation error is selected and other approaches are discarded. The lowest average validation error does not necessarily guarantee the lowest individual validation error for a given location. It might be the case that a transform with a higher average validation error yields the lowest individual validation error at a particular location but for a true blind test location there is no way to measure the individual estimation error other than actually drilling. For this study well 6507/11-11 was selected as true blind location. It can be seen that for this particular location, the transform with the lowest average validation error (low-frequency estimates using conventional LFM built using a single well as attribute) is also the one closest to the actual low-frequency P-Impedance values of the log. Any other approach yields far worse estimates.

The question to be answered is whether or not the multiattribute transform with the lowest average validation error can yield better P-impedance estimates than the traditional approach. A visual inspection of the results shown in figure 5.1 demonstrates that the multiattribute derived estimates resemble much better the P-Impedance variation with depth than the traditional approach. More over, the RMS estimation error between the conventional low-frequency model and the actual low-pass filtered log is 791 $(m/s) * (g/cc)$, whereas between the multiattribute derived values is 519 $(m/s) * (g/cc)$, which is around 270 $(m/s) * (g/cc)$ lower than the conventional method. Then, for low-frequency P-Impedance, machine learning represents an improvement over the traditional method.

When it comes down to $V_P/V_S$ or S-Impedance, it is required to have shear-wave velocity knowledge. Towed-streamers seismic can be broadband but cannot measure S-wave velocities as oppose for P-wave velocities. Only ocean-bottom seismic can measure S-wave velocities but this seismic represents a small fraction of the total marine seismic acquired to date. Even when ocean-bottom seismic is available, the current state of Full-Waveform Inversion relies on the solution of the acoustic wave equation. To properly model the full physics of wave propagation, solutions to the elastic wave equation are required. Current efforts are focused in that direction (Manukyan et al., 2016). P-wave velocity can be converted to S-wave velocity using Castagna et al. (1985)'s mudrock line for example. This conversion is not straightforward as this relation varies not only by facies but with other parameters as depth and fluid content. Here is the concept of joint-facies inversion better captures the physics of the problem. All these facts increase the uncertainty of S-wave related estimates compared to the P-wave estimates counterpart.

For this particular study, only two wells contain S-wave information as mentioned in the methodology chapter, as opposed to P-wave that five wells were available. This is a big drawback for any machine learning scheme. Ross (2002) mentions that any statistical correlation using wells and neural networks should be used when at least five or more wells are available, otherwise the training lacks of statistical robustness. This means that neural networks are far more effective under development or characterization contexts than prospecting or exploration contexts. To illustrate how much of a difference one less available well can make, observe the difference between average training error and average validation error for table 4.4 using the optimum number of attributes that is seven. The average training error is around two thirds of the average validation error. It is important to recall that the average training error is the average estimation error between the estimates values and the actual values using all available wells, and the average validation error is the average estimation error using all available wells but leaving a different one out for validation only (not for training the data). Then the error difference between average training error and average validation error is basically the error difference given by losing estimation power due to using one less well in the training. This example is for the training with the lowest validation error for P-Impedance where a total of 5 wells are available. Again, it is important to emphasize that only 2 wells that contain S-wave information are available.

The multiattribute transform with the lowest average validation error is given by estimat-

ing low-frequency $V_P/V_S$ values using conventional LFM built using a single well as attribute. Results in figure 5.1 show that low-frequency $V_P/V_S$ and S-Impedance are not robust when compared to P-Impedance estimates. The RMS estimation error between the conventional low-frequency model and the actual low-pass filtered log is 0.26, whereas between the multiattribute derived values is 0.36, which is 0.1 higher than the conventional method. Then, for low-frequency $V_P/V_S$, machine learning assisted low-frequency modelling does not represent an improvement over the traditional method. The same applies for S-Impedance, where a conventional LFM using a single well was not built. In this case the RMS estimation error between the conventional low-frequency model and the actual low-pass filtered log is 660 $(m/s)*(g/cc)$, whereas between the multiattribute derived values is 931 $(m/s)*(g/cc)$, which is around 260 $(m/s)*(g/cc)$ higher than the conventional method. This was expected as mentioned before due to the reduced number of wells containing S-wave information. The problem is extremely under-determined for $V_P/V_S$ and S-Impedance for the multiattribute derived estimates to be reliable. One question to be answered in future work is how better the multiattribute derived $V_P/V_S$ and S-Impedance low-frequency models can be if at least five wells containing S-wave information were available.

Another point to discuss is that Neural Networks are designed by definition to estimate stationary (trendless) data series. This means that Neural Networks work better to estimate values within the same formation where the values are almost trendless. In other words, Neural Networks work better to estimate absolute values per facies. The non-linear relation between target log and attributes for a given facies might be totally different for a given setting. This is compensated by cascading the Neural Networking training with multi-linear regression as described in the methodology chapter. As a matter of fact, multi-linear regression alone estimates better the low-frequency content of the target log than the PNN alone. However, cascading the multi-linear regression used in step-wise regression with the PNN is the optimal approach. This fact reinforces that the concept of inverting per facies is a more proper way to capture the physics of the inversion problem as described in the introduction.

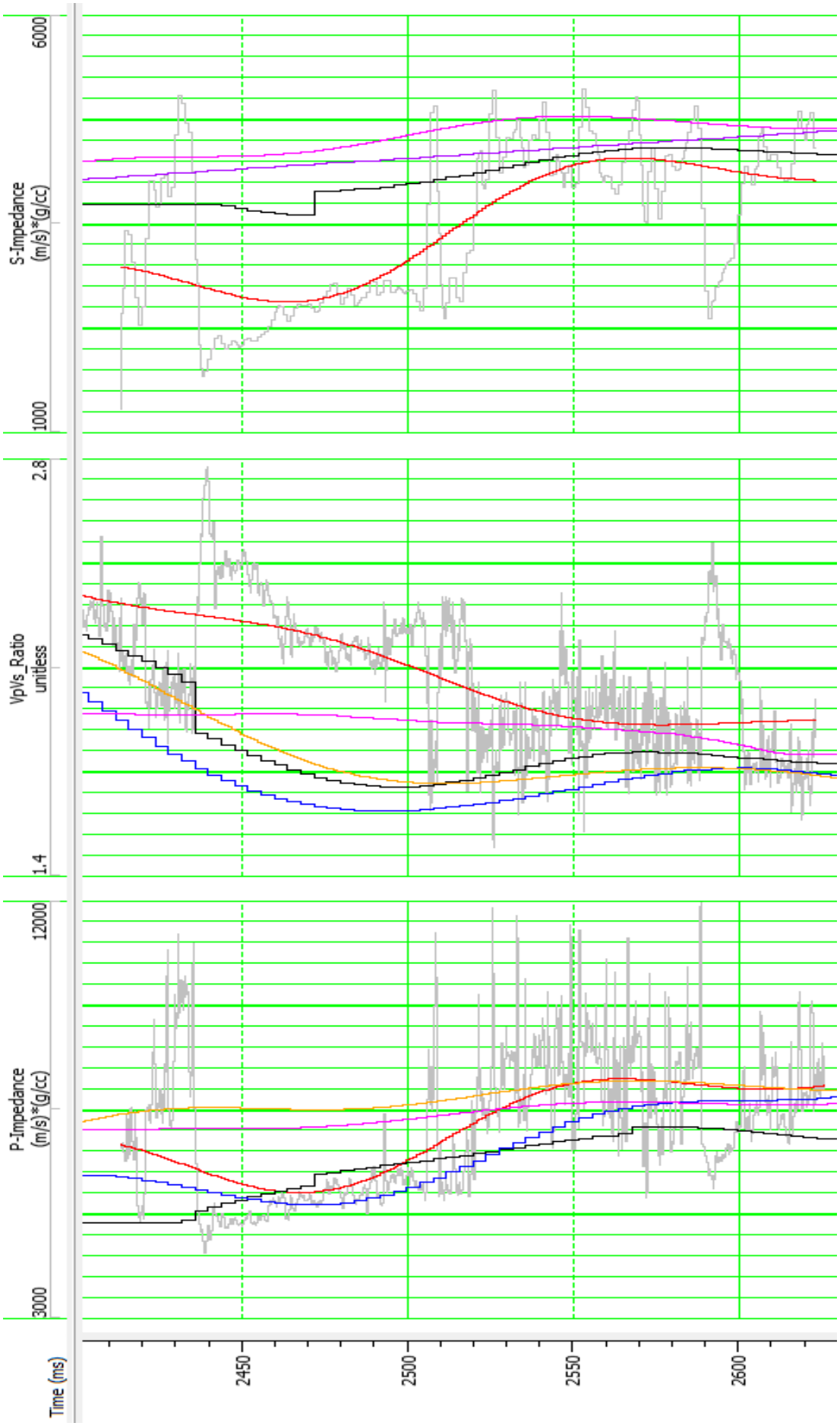


**Figure 5.1:** Conventional low-frequency model and multiattribute transforms comparison for P-Impedance, $V_P/V_S$, and S-Impedance at true blind test location 6507/11-11. Actual log in grey, low-pass filtered log in red, conventional low-frequency model in black, low-frequency estimates using conventional LFM built using a single well as attribute in blue, low-pass filtered absolute estimates using conventional LFM built using a single well as attribute in yellow, low-pass filtered absolute estimates using trendless data only in pink, and low-frequency estimates using trendless data only in purple.

# Chapter 6

# Conclusions

It has been demonstrated that the methodology proposed in this study for building low-frequency models of elastic properties using multiattribute analysis based on Neural Networks represents an improvement over the conventional low-frequency model building method.

Even though the proposed methodology has the potential to estimate more accurately the low-frequency content of an elastic property away from well control than the standard interpolation and extrapolation guided by interpreted horizons and faults, the accuracy of the estimates depends on the quality of the seismic data, well log data, well-to-seismic tie, frequency content of the seismic data, available seismic attributes, number of available wells, training parameters, and what formations and facies are logged.

Broadband prestack seismic data was available. Excellent well-to-seismic ties was performed. Relevant attributes with justifiable physical relationship with elastic properties were used for the Neural Network training, including AVO attributes and relative impedance. Stepwise regression and crossvalidation were used to optimize the training parameters.

P-impedance estimates were more accurate than S-wave related estimates. This is explained by the fact that the number of wells and formation/facies logged containing S-wave information was quite limited compared to those containing P-wave information. If the conditions are met, the described methodology yields more robust low-frequency models hence resulting in more accurate absolute estimates from AVO inversion. More accurate velocity fields from Full-Waveform inversion could be benefitial to improve the accuracy of P-Impedance but the challenge is to quantify how well the conditions are satisfied in practical exploration cases, particularly for S-wave related estimates.

# Bibliography


Aki, K. and Richards, P. G. (1980). Quantitative seismology: Theory and methods. *W.H Freeman and Co*.

Avseth, P., Janke, A., and Horn, F. (2016). Avo inversion in exploration — key learnings from a norwegian sea prospect. *The Leading Edge*, 35(5):405–414.

Avseth, P., Mukerji, T., and Mavko, G. (2005). Quantitative seismic interpretation: Applying rock physics tools to reduce interpretation risk. *Cambridge university press*.

Ball, V., Blangy, J., Schiott, C., and Chaveste, A. (2014). Relative rock physics. *The Leading Edge*, 33(3):276–286.

Ball, V., Tenorio, L., Schiott, C., Blangy, J. P., and Thomas, M. (2015). Uncertainty in inverted elastic properties resulting from uncertainty in the low-frequency model. *The Leading Edge*, 34(9):1028–1035.

Banchs, R. E. and Michelena, R. J. (2002). From 3d seismic atrributes to pseudo-well-log volumes using neural networks: Practical considerations. *The Leading Edge*, 21(10):996–1001.

Castagna, J. P., Batzle, M. L., and Eastwood, R. L. (1985). Relationships between compressional-wave and shear-wave velocities in clastic silicate rocks. *GEOPHYSICS*, 50(4):571–581.

Castagna, J. P. and Smith, S. W. (1994). Comparison of avo indicators: A modeling study. *GEOPHYSICS*, 59(12):1849–1855.

Castagna, J. P., Swan, H. W., and Foster, D. J. (1998). Framework for avo gradient and intercept interpretation. *GEOPHYSICS*, 63(3):948–956.

Cerney, B. and Bartel, D. C. (2007). Uncertainties in low-frequency acoustic impedance models. *The Leading Edge*, 26(1):74–87.

Chen, T., Khaled, O., Ebrahim, M., Hafez, M., and Mohammed, I. S. (2015). Lithology prediction of burgan formation using prestack simultaneous inversion combined with statistical method: A case study in north kuwait. *SEG Technical Program Expanded Abstracts 2015*.

Chopra, S. and Castagna, J. (2014). Avo. *Investigations in Geophysics No.16, Society of Exploration Geophysicists*.

Chopra, S. and Marfurt, K. (2007). Seismic attributes for prospect identification and reservoir characterization. *Society of Exploration Geophysicists and European Association of Geoscientists and Engineers*.

Connolly, P. (1999). Elastic impedance. *The Leading Edge*, 18(4):438–452.

Cooke, D. and Cant, J. (2010). Model-based seismic inversion: Comparing deterministic and probabilistic approaches. *CSEG Recorder*, 35(4):29–39.

Cooke, D., Sena, A., Mauko, G., Muryanto, T., Ball, V., et al. (1999). What is the best seismic attribute for quantitative seismic reservoir characterization? *SEG Technical Program Expanded Abstracts 1999*.

Fatti, J. L., Smith, G. C., Vail, P. J., Strauss, P. J., and Levitt, P. R. (1994). Detection of gas in sandstone reservoirs using avo analysis: A 3-d seismic case history using the geostack technique. *GEOPHYSICS*, 59(9):1362–1376.

Francis, A. (2006). Understanding stochastic inversion: Part 1. *First Break*, 24(11):69–77.

Francis, A. (2010). Limitations of deterministic seismic inversion data as input for reservoir model conditioning. pages 2396–2400.

Goodway, B., Chen, T., and Downton, J. (1997). Improved avo fluid detection and lithology discrimination using lamé petrophysical parameters;"$\lambda\rho$", $\mu\rho$, $\lambda$ $\mu$ fluid stack", from p and s inversions. *SEG Technical Program Expanded Abstracts 1997*.

Hampson, D. P., Schuelke, J. S., and Quirein, J. A. (2001). Use of multiattribute transforms to predict log properties from seismic data. *GEOPHYSICS*, 66(1):220–236.

Hansen, T. M., Mosegaard, K., Pedersen-Tatalovic, R., Uldall, A., and Jacobsen, N. L. (2008). Attribute-guided well-log interpolation applied to low-frequency impedance estimation. *GEOPHYSICS*, 73(6):R83–R95.

Herrera, V. M., Russell, B., and Flores, A. (2006). Neural networks in reservoir characterization. *The Leading Edge*, 25(4):402–411.

Kalkomey, C. T. (1997). Potential risks when using seismic attributes as predictors of reservoir properties. *The Leading Edge*, 16(3):247–251.

Kelly, M., Skidmore, C., and Ford, D. (2001). Avo inversion, part 1: Isolating rock property contrasts. *The Leading Edge*, 20(3):320–323.

Kemper, M. and Gunning, J. (2014). Joint impedance and facies inversion–seismic inversion redefined. *First Break*, 32(9):89–95.

Keynejad, S., Sbar, M. L., and Johnson, R. A. (2017). Comparison of model-based generalized regression neural network and prestack inversion in predicting poisson's ratio in heidrun field, north sea. *The Leading Edge*, 36(11):938–946.

Lancaster, S. and Whitcombe, D. (2000). Fast-track 'coloured' inversion. *SEG Technical Program Expanded Abstracts 2000*.

Leiphart, D. J. and Hart, B. S. (2001). Comparison of linear regression and a probabilistic neural network to predict porosity from 3-d seismic attributes in lower brushy canyon channeled sandstones, southeast new mexico. *GEOPHYSICS*, 66(5):1349–1358.

Li, Y., Downton, J., and Xu, Y. (2007). Practical aspects of avo modeling. *The Leading Edge*, 26(3):295–311.

Li-ping, W. and Han-ming, G. (2014). Using prestack simultaneous inversion based on bayes' theorem for meticulous characterization of ordovician fractured-vuggy carbonate reservoir. *SEG Technical Program Expanded Abstracts 2014*.

Lines, L. R. (1998). Density contrast is difficult to determine from avo. *Consortium for Research in Elastic Wave Exploration Seismology Research Report*, 10.

Liu, Z. and Liu, J. (1998). Seismic-controlled nonlinear extrapolation of well parameters using neural networks. *GEOPHYSICS*, 63(6):2035–2041.

Ma, X. (2002). Simultaneous inversion of prestack seismic data for rock properties using simulated annealing. *GEOPHYSICS*, 67(6):1877–1885.

Ma, Y. Z. (2011). Pitfalls in predictions of rock properties using multivariate analysis and regression methods. *Journal of Applied Geophysics*, 75(2):390–400.

Ma, Y. Z. and Gomez, E. (2015). Uses and abuses in applying neural networks for predictions in hydrocarbon resource evaluation. *Journal of Petroleum Science and Engineering*, 133:66–75.

Mahob, P. N. and Castagna, J. P. (2003). Avo polarization and hodograms: Avo strength and polarization product. *GEOPHYSICS*, 68(3):849–862.

Mallick, S. and Fu, D. (2007). Seismic inversion with accuracy and efficiency. *SEG Technical Program Expanded Abstracts 2007*.

Mancini, F., Prindle, K., Ridsdill-Smith, T., and Moss, J. (2016). Full-waveform inversion as a game changer: Are we there yet? *The Leading Edge*, 35(5):445–451.

Manukyan, E., Maurer, H., and Nuber, A. (2016). Improvements to elastic full waveform inversion using cross-gradient constraints. pages 1506–1510.

Nanda, N. C. (2016). Seismic data interpretation and evaluation for hydrocarbon exploration and production: A practitioner's guide. *Springer*.

Neter, J., Kutner, M. H., Nachtsheim, C. J., and Wasserman, W. (1996). Applied linear statistical models. *Irwin Chicago*.

Özdemir, H. (2009). Unbiased deterministic seismic inversion: More seismic, less model. *first break*, 27(11):43–50.

Pendrel, J. (2015). Low frequency models for seismic inversions: strategies for success. pages 2703–2707.

Pendrel, J., Debeye, H., Pedersen-Tatalovic, R., Goodway, B., Dufour, J., Bogaards, M., Stewart, R. R., et al. (2000). Estimation and interpretation of p and s impedance volumes from simultaneous inversion of pwave offset seismic data. *SEG Technical Program Expanded Abstracts 2000*.

Poulton, M. M. (2002). Neural networks as an intelligence amplification tool: A review of applications. *GEOPHYSICS*, 67(3):979–993.

Quakenbush, M., Shang, B., and Tuttle, C. (2006). Poisson impedance. *The Leading Edge*, 25(2):128–138.

Ray, A. K. and Chopra, S. (2015). More robust methods of low-frequency model building for seismic impedance inversion. *SEG Technical Program Expanded Abstracts 2015*.

Rimstad, K., Avseth, P., and Omre, H. (2012). Hierarchical bayesian lithology/fluid prediction: A north sea case study. *GEOPHYSICS*, 77(2):B69–B85.

Ross, C. P. (2002). Comparison of popular avo attributes, avo inversion, and calibrated avo predictions. *The Leading Edge*, 21(3):244–252.

Ross, C. P. and Kinman, D. L. (1995). Nonbright-spot avo: Two examples. *GEOPHYSICS*, 60(5):1398–1408.

Roy, B., Anno, P., and Gurch, M. (2008). Imaging oil-sand reservoir heterogeneities using wide-angle prestack seismic inversion. *The Leading Edge*, 27(9):1192–1201.

Russell, B. (2012). Making sense of all that avo stuff. *ASEG Extended Abstracts 2012: 22nd Geophysical Conference*.

Rüger, A. (2002). Reflection coefficients and azimuthal avo analysis in anisotropic media. *Society of Exploration Geophysicists*.

Sams, M. and Carter, D. (2017). Stuck between a rock and a reflection: A tutorial on low-frequency models for seismic inversion. *Interpretation*, 5(2):B17–B27.

Schultz, P. S., Ronen, S., Hattori, M., and Corbett, C. (1994). Seismic-guided estimation of log properties (part 1: A data-driven interpretation methodology). *The Leading Edge*, 13(5):305–310.

Schuster, G. (2017). Seismic inversion. *Society of Exploration Geophysicists*.

Simm, R. and Bacon, M. (2014). Seismic amplitude: An interpreter's handbook. *Cambridge University Press*.

Skidmore, C., Kelly, M., and Cotton, R. (2001). Avo inversion, part 2: Isolating rock property contrasts. *The Leading Edge*, 20(4):425–428.

Smith, G. and Gidlow, P. (1987). Weighted stacking for rock property estimation and detection of gas. *Geophysical Prospecting*, 35(9):993–1014.

Specht, D. F. (1990). Probabilistic neural networks. *Neural networks*, 3(1):109–118.

Stovas, A., Landrø, M., and Avseth, P. (2005). Estimation of net-to-gross and fluid saturation in a fine-layered sand-shale sequence — tested on offshore brazil data. pages 228–231.

Taner, M. T., Schuelke, J. S., O'Doherty, R., and Baysal, E. (2005). Seismic attributes revisited. pages 1104–1106.

van der Baan, M. and Jutten, C. (2000). Neural networks in geophysical applications. *GEOPHYSICS*, 65(4):1032–1047.

Veeken, P., Silva, D., and M (2004). Seismic inversion methods and some of their constraints. *First break*, 22(6):47–70.

Whitcombe, D. N., Connolly, P. A., Reagan, R. L., and Redshaw, T. C. (2002). Extended elastic impedance for fluid and lithology prediction. *GEOPHYSICS*, 67(1):63–67.

White, R. and Simm, R. (2003). Tutorial: Good practice in well ties. *First Break*, 21(10).

Wiggins, R., Kenny, G., and McClure, C. (1983). A method for determining and displaying the shear-velocity reflectivities of a geologic formation. *European patent application*, 113944.

Xia, Q., Tian, L., Zhou, D., et al. (2012). Low frequency model building based on relative impedance inversion to improve the accuracy of pre-stack simultaneous inversion: A case study from r oilfield in bohai bay, china. *SEG Technical Program Expanded Abstracts 2012*.

Yenwongfai, H. D., Mondol, N. H., Faleide, J. I., and Lecomte, I. (2017a). Prestack simultaneous inversion to predict lithology and pore fluid in the realgrunnen subgroup of the goliat field, southwestern barents sea. *Interpretation*, 5(2):SE75–SE96.

Yenwongfai, H. D., Mondol, N. H., Faleide, J. I., Lecomte, I., and Leutscher, J. (2017b). Prestack inversion and multiattribute analysis for porosity, shale volume, and sand probability in the havert formation of the goliat field, southwest barents sea. *Interpretation*, 5(3):SL69–SL87.

Zou, Z., Ling, Y., Wang, Y., Gao, J., and Xi, X. (2013). Low-frequency impedance modeling based on well logs and seismic attributes. *75th EAGE Conference & Exhibition incorporating SPE EUROPEC 2013*.